

APPLICATION OF SHARK SKIN FLOW
CONTROL TECHNIQUES
TO AIRFLOW

by

JACKSON ALEXANDER MORRIS

AMY W. LANG, COMMITTEE CHAIR
JAMES P. HUBNER
DAVID W. MACPHEE

A THESIS

Submitted in partial fulfillment of the requirements
for the degree of Master of Science in the Department
of Aerospace Engineering and Mechanics
in the Graduate School of
The University of Alabama

TUSCALOOSA, ALABAMA

2017

Copyright Jackson Alexander Morris 2017
ALL RIGHTS RESERVED

ABSTRACT

Due to millions of years of evolution, sharks have evolved to become quick and efficient ocean apex predators. Shark skin is made up of millions of microscopic scales, or denticles, that are approximately 0.2 mm in size. Scales located on the shark's body where separation control is paramount (such as behind the gills or the trailing edge of the pectoral fin) are capable of bristling. These scales are hypothesized to act as a flow control mechanism capable of being passively actuated by reversed flow. It is believed that shark scales are strategically sized to interact with the lower 5% of a boundary layer, where reversed flow occurs at the onset of boundary layer separation. Previous research has shown shark skin to be capable of controlling separation in water. This thesis aims to investigate the same passive flow control techniques in air.

To investigate this phenomenon, several sets of microflaps were designed and manufactured with a 3D printer. The microflaps were designed in both 2D (rectangular) and 3D (mirroring shark scale geometry) variants. These microflaps were placed in a low-speed wind tunnel in the lower 5% of the boundary layer. Solid fences and a flat plate diffuser with suction were placed in the tunnel to create different separated flow regions. A hot film probe was used to measure velocity magnitude in the streamwise plane of the separated regions. The results showed that low-speed airflow is capable of bristling objects in the boundary layer. When placed in a region of reverse flow, the microflaps were passively actuated. Microflaps fluctuated between bristled and flat states in reverse flow regions located close to the reattachment zone.

LIST OF ABBREVIATIONS AND SYMBOLS

A	=	Calibration coefficient
c	=	Chord length
C_p	=	Pressure coefficient
D_h	=	Hydraulic diameter
f	=	Frequency
H	=	Nondimensional fence height
k	=	Roughness coefficient
l_v	=	Viscous length scale
M_c	=	Moment coefficient
M_q	=	Moment due to dynamic pressure
M_{Fr}	=	Moment due to friction
P	=	Static pressure
P_0	=	Total (stagnation) pressure
P_{0fs}	=	Free-stream stagnation pressure
ΔP	=	Pressure change
\dot{Q}	=	Dimensionless suction flow rate
Q_s	=	Volumetric suction flow rate
R	=	Specific gas constant

Re	=	Reynolds number
Re_H	=	Reynolds number based on fence height
St	=	Strouhal number
T	=	Temperature
t	=	Time
t_ν	=	Viscous time scale
u	=	Local velocity
u_∞	=	Free-stream velocity
u_*	=	Friction velocity
V	=	Voltage
x, y, z	=	Cartesian wind tunnel coordinates (Fig. 2.32)
y^+	=	Wall unit
δ	=	Boundary layer height
λ	=	Darcy-Weisbach coefficient
μ	=	Dynamic viscosity
ν	=	Kinematic viscosity
ξ	=	Minor loss coefficient
ρ	=	Density
τ	=	Shear stress
τ_w	=	Shear stress at the wall

ACKNOWLEDGEMENTS

First, I would like to thank the members of my thesis committee, Dr. Amy Lang, Dr. James Paul Hubner, and Dr. David MacPhee, for their dedication to my research. For the past 18 months they have acted as advisors on this project, offering their guidance and personal advice through every step of the way. Dr. Lang and Dr. Hubner's support of me goes back far longer; they guided and supported me from the moment I attended the University of Alabama and embarked on my goal to become an aerospace engineer.

None of this research would have been possible without the help of my partner, Sean Devey. I absolutely must thank him for his essential work in the design of the shark skin models. His accurate and innovative modeling work truly enabled this project to succeed. His hard work and advice provided every day also personally helped me throughout this research.

I would like to thank the hardworking men in the University of Alabama machine shop and 3D manufacturing lab for truly being the building blocks of the experiments performed, their help in redesigns and concepts, and willingness to always help my project succeed by helping behind the scenes in every way they could. I would like to especially thank Tim Connel, Bobby "Jim" Edmonds, James Yarbrough, and Doug Cannon.

I would like to thank my family, professors, Ashley, and all my friends at the University of Alabama and elsewhere for always believing in me. I would never have made it this far without you.

Finally, I would like to thank you, the reader, for taking the time to read this thesis. I hope it can help to make a difference in whatever you wish to achieve.

CONTENTS

ABSTRACT.....	ii
LIST OF ABBREVIATIONS AND SYMBOLS	iii
ACKNOWLEDGEMENTS	v
LIST OF TABLES	viii
LIST OF FIGURES	ix
CHAPTER 1: INTRODUCTION.....	1
1.1 An Introduction to Flow Control	1
1.2 Fluid Characteristics, Separation, and the Structure of the Boundary Layer.....	2
1.3 Mechanisms of Flow Control.....	10
1.4 Shark Skin Morphology and Flow Control.....	13
1.5 Summary and Objectives	20
CHAPTER 2: SHARK SKIN MODEL DESIGN AND EXPERIMENTAL SETUP	23
2.1 Experimental Facilities	23
2.2 Microflap Design Process	31
2.3 Flat Plate Diffuser to Induce Separation.....	38
2.4 Solid Fence to Induce Separation	44
2.5 Test Procedures.....	47
CHAPTER 3: RESULTS AND DISCUSSION.....	54

3.1 2D Microflap Results	54
3.2 3D Microflap Bristling Results	58
3.3 Fence Downstream Velocity Profiles	62
3.4 3D Microflap Fence Results	66
3.3.1 Results 1H Downstream of Fence.....	66
3.3.2 Results 2.66 Downstream of Fence	67
3.3.3 Results 4H Downstream of Fence.....	69
3.3.4 Results 8H Downstream of Fence.....	70
3.3.5 Results 12H Downstream of Fence.....	72
3.3.6 Results Upstream of Fence	77
3.4 Suction Plate Results.....	78
3.4.1 Tuft Results	79
3.4.2 Combination Flat Plate and Fence Results	80
3.5 Summary and Microflap Bristling and Fluctuation Analysis	83
CHAPTER 4: CONCLUSIONS	88
REFERENCES	90

LIST OF TABLES

Table 1. Physical properties of 3D printing material VeroClear.....	37
Table 2. Estimated flow rate through flat plate diffuser	43
Table 3. Reynolds number and boundary layer thickness ratios of solid fences in test section ..	46
Table 4. Total test matrix	53

LIST OF FIGURES

Figure 1.1 Graphical representation of the boundary layer (Anderson, 2010)	3
Figure 1.2 Evolution of separated flow in an adverse pressure gradient (Anderson, 2010)	4
Figure 1.3 Visualization of separated flow over a sphere (van Dyke, 1982).....	5
Figure 1.4 Turbulent energy production rate at different wall heights (Kline <i>et al</i> , 1976).....	6
Figure 1.5 Lifting and bursting process of a low-speed streak (Blackwelder and Eckelmann, 1978)	9
Figure 1.6 Bubble time line visualization of low-speed streak, side view. Wire is placed $5 y^+$ from the wall, timeline generation is 30 Hz (Smith <i>et al</i> , 2012)	9
Figure 1.7 Buffer layer turbulence increase inside a dimple on a sphere (Choi <i>et al</i> , 2006).....	11
Figure 1.8 Mako scale variants at approximately 200x magnification. Scales A1-A3 are located in posterior region, B1-B6 gills region, C1-C3 tail region, and P1-P3 pectoral fin (Motta <i>et al</i> , 2012)	14
Figure 1.9 Scanning electron microscope image of mako scales. Left image is resting position; right image has been manually bristled (Lang <i>et al</i> , 2014).....	15
Figure 1.10 Average maximum bristling angle of mako scales (Lang <i>et al</i> , 2011).....	15
Figure 1.11 Particle ejection from cavity into the boundary layer at 0.38 m/s. Each row is a separate sequence from left to right (Wheelus, 2015)	17
Figure 1.12 Actuation of a single scale due to water jet. Scale is unbristled on left and fully bristled on right (Wheelus, 2015)	18
Figure 1.13 Time-averaged backflow coefficient color contour over smooth and shark skin-covered hydrofoils at 0.32 m/s (Lang <i>et al</i> , 2014).....	19
Figure 2.1 Schematic of wind tunnel layout	24
Figure 2.2 Schematic of boundary layer probe and linear traverse	25
Figure 2.3 Boundary layer probe	25

Figure 2.4 Locations of BL probe tests. Adjustable ceiling was set to flat for all tests, resulting in constant cross-sectional area for test section	26
Figure 2.5 Velocity distributions in boundary layer, panel 1	27
Figure 2.6 Velocity distributions in boundary layer, panel 5.....	28
Figure 2.7 Velocity distributions in boundary layer, panel 8.....	28
Figure 2.8 Nondimensionalized velocity distribution in boundary layer, panel 8 at 15 m/s	29
Figure 2.9 Pressure coefficient measurements along test section at 30 m/s, with standard deviation error bars	30
Figure 2.10 Measured boundary layer height and 5 th order estimation	31
Figure 2.11 Array of scales located on the flank region of the mako shark (Motta <i>et al</i> , 2012) .	32
Figure 2.12 Side view of 2D microflap model with CG (A), isometric view of 2D microflap model with longitudinal riblets (B), 2D microflap model array at rest (C), 2D microflap array model showing rotation, (D).....	33
Figure 2.13 CAD model of 3D microflap design.....	34
Figure 2.14 Scanning electron microscope images of individual mako flank scales (Lang <i>et al</i> , 2011).....	34
Figure 2.15 Magnification of printed 3D microflap.	35
Figure 2.16 CAD model of pre-bristled 3D microflap array	35
Figure 2.17 Completed array of 2D microflaps	36
Figure 2.18 Completed array of 3D microflaps	37
Figure 2.19 Schematic of flat plate with suction	40
Figure 2.20 Rear view of plate and suction tubes	40
Figure 2.21 CDF 1000H performance data specified by manufacturer	41
Figure 2.22 CDF 1000H venturi	42
Figure 2.23 Vacuum pressure between wind tunnel and plenum chamber	43
Figure 2.24 Estimated flow rate through flat plate diffuser	44
Figure 2.25 Velocity measurements behind a 5 cm fence at 10 m/s (van Ratingen <i>et al</i> , 2013).	45

Figure 2.26 3.8 cm fence placed in wind tunnel test section	46
Figure 2.27 2D microflaps placed in reverse orientation.....	47
Figure 2.28 Pre-bristled 2D microflaps.....	48
Figure 2.29 3D microflaps 4H downstream of 3.8 cm fence.....	49
Figure 2.30 3D microflaps underneath flat plate diffuser.....	50
Figure 2.31 3D microflaps upstream of 3.8 cm fence.....	51
Figure 2.32 Schematic of hot film probe behind solid fence	51
Figure 3.1 0.5 second time-lapse of 2D microflap bristling and downstream microflap dropping	55
Figure 3.2 Alternating pattern of pre-bristled 2D microflaps being pushed down by flow.....	56
Figure 3.3 Pre-bristled 2D microflaps pushed down at 27 m/s.....	56
Figure 3.4 3D microflaps bristled by reverse flow at various speeds. 10 m/s (A), 20 m/s (B), 25 m/s (C), and 30 m/s (D)	59
Figure 3.5 Pre-bristled 3D microflaps at 30 m/s; most microflaps are not pushed down.....	61
Figure 3.6 Nondimensionalized velocity profiles at 1H vertical distance with standard deviation error bars	63
Figure 3.7 Velocity measurements behind a 5 cm fence at 10 m/s (van Ratingen <i>et al</i> , 2013)...	63
Figure 3.8 Nondimensionalized velocity profiles at 0.5H vertical distance with standard deviation error bars	64
Figure 3.9 Nondimensionalized velocity profiles at 0.15H vertical distance with standard deviation error bars	65
Figure 3.10 3D microflaps 1H downstream of a 3.8 cm fence at 25 m/s	67
Figure 3.11 3D microflaps 2.66H downstream of a 1.9 cm fence at 25 m/s. Half of the microflaps are fully bristled.....	68
Figure 3.12 3D microflaps 2.66H downstream of a 3.8 cm fence. Test velocity is 20 m/s (A) and 30 m/s (B)	68
Figure 3.13 3D microflaps 4H downstream of a 3.8 cm fence. 15 m/s (A), 20 m/s (B), 30 m/s (C)	69

Figure 3.14 3D microflaps 8H downstream of a 3.8 cm fence. 10 m/s (A), 15 m/s (B), 20 m/s (C), 30 m/s (D), top left to bottom right.....	72
Figure 3.15 Multiple images of fluctuating 3D microflaps 12H downstream of a 1.9 cm fence at 20 m/s	73
Figure 3.16 Multiple images of fluctuating 3D microflaps 12H downstream of a 1.9 cm fence at 30 m/s	74
Figure 3.17 Fluctuating 3D microflaps 12H downstream of a 3.8 cm fence at 18 m/s	75
Figure 3.18 Multiple images of fluctuating 3D microflaps 12H downstream of a 3.8 cm fence at 25 m/s	76
Figure 3.19 3D microflaps upstream of 1.9 cm fence at 30 m/s	77
Figure 3.20 3D microflaps upstream of 3.8 cm fence at 30 m/s	78
Figure 3.21 3D microflaps upstream of a 3.8 cm fence, at 130% chord length of flat plate set at 13°. 10 m/s and 1300 L/min of suction	81
Figure 3.22 3D microflaps upstream of a 3.8 cm fence at 130% chord length of flat plate set at 13°. 15 m/s with no suction (A), 800 L/min of suction (B), and 2000 L/min of suction (C)	82
Figure 3.23 View of 3D microflaps upstream of a 3.8 cm fence, at 130% of flat plate at 13°. 20 m/s with 2000 L/min of suction.	83
Figure 3.24 Schematic of expected flow behavior and observed microflap behavior upstream and downstream of 2D fence.....	84
Figure 3.25 Moment coefficient applied to 3D microflaps downstream of 3.8 cm fence	86

CHAPTER 1: INTRODUCTION

1.1 An Introduction to Flow Control

Mankind has possessed the ability of powered, controlled flight for over 100 years. Thanks to technological advancements, aircraft have become safer, faster, and more efficient. A major goal of engineers to improve aircraft efficiency is to minimize the resistive force on aircraft: drag. One way to reduce drag is through flow control or by altering the behavior of a fluid so that it behaves more favorably than what would occur naturally.

Powered flight is a relatively young practice, but the art of flow control can be traced back much farther. Prehistoric spears and arrows implement flow control techniques such as shaping and fins (Dennel, 1997). Although the science was not understood at the time, early humans realized that objects that interacted with air could be altered to improve performance. Shark scales are an example of how nature may have been using flow control techniques for millions of years. In a modern sense, the science of flow control begins with Prandtl's 1904 paper "*On Fluid Motion with Very Small Friction*" (1904), which introduced the concept of the boundary layer, separation, and methods of controlling fluid flow (Gad-El-Hak, 2000).

Flow control can be generally divided into two categories: passive and active. Passive flow control systems require no energy expenditure to control flow and usually involve geometrical modification, such as the use of vortex generators and riblets on wings or dimples on a golf ball (Choi, 2006). These systems are usually simple to implement and are typically

designed to reduce drag as much as possible. However, differing flow conditions on a passive device may increase drag.

Active flow control, on the other hand, can be switched off when not needed and switched on when it can provide a drag reduction. Examples include dynamic flaps, actuated jet nozzles, or suction systems. Active flow control requires energy to activate the flow control device and often requires additional computer control to ensure that flow control devices are engaged at the right moments. One advantage of this is that active devices can be customized and tuned for specific scenarios, potentially leading to greater drag reductions.

An ideal flow control system would be both passive (able to reduce drag without spending energy) and flow-actuated (the flow conditions cause the control system to engage only when needed). However, in engineering, compromises must always be made, and flow control systems will usually have some downsides, such as being too complex to implement on a vehicle, being too costly, or having too much of a weight penalty.

1.2 Fluid Characteristics, Separation, and the Structure of the Boundary Layer

Flow control is needed due to the desire to create favorable conditions over objects that interact with fluids. Before discussing flow control, a general background is needed in the fluid behaviors that make flow control necessary. These include the development of boundary layers, flow separation, and forces over objects that move through fluid.

The boundary layer is a region of low-speed fluid that forms very close to a surface, such as over a flat plate. At the surface of the plate, friction mandates a no-slip condition, or that particle velocity at the surface is equal to zero (relative to the surface). Although there is no fluid motion at the surface, the fluid exerts a tangential friction force on the plate in the direction of

fluid motion. This force over area is represented by shear stress, τ . At some distance δ away from the plate, the fluid particles move at the local free-stream velocity u . Just as the fluid exerts shear stress on the surface, the surface exerts an equal and opposite force on the fluid particles. This reaction force acts on all fluid particles between the surface of the plate and δ . This region is defined as the boundary layer. Within the boundary layer, all fluid particles are retarded by the reaction force and move slower than the local free-stream velocity (Anderson, 2010). Fig. 1.1 (Anderson, 2010) shows a representation of the boundary layer.

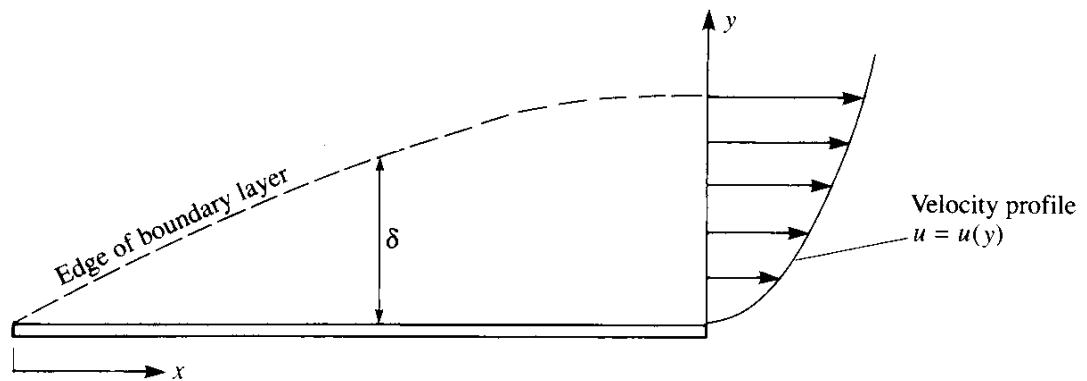


Figure 1.1 Graphical representation of the boundary layer (Anderson, 2010)

The existence of low-momentum flow in the boundary layer introduces another aspect of drag production: separation. In some situations, ambient pressure increases the farther downstream the flow moves. This is called an adverse pressure gradient. Flow in the boundary layer is already slowed by friction; the opposing force provided by the adverse pressure gradient reduces the flow velocity further. If the adverse pressure gradient is strong enough, the boundary layer flow velocity reaches zero and eventually reverses.

A no-slip condition still exists at the surface, but due to the reverse flow region a second point of zero velocity now exists in the boundary layer some height above the surface (where

flow velocity changes from reversed to forwards). In a sense, flow has “separated” from the surface: the point where the forward flow boundary layer begins is no longer on the surface but some distance away from it. Fig. 1.2 (Anderson, 2010) shows the principle of an adverse pressure gradient inducing separation over an object. Fig. 1.3 (van Dyke, 1982) shows separated flow over a sphere.

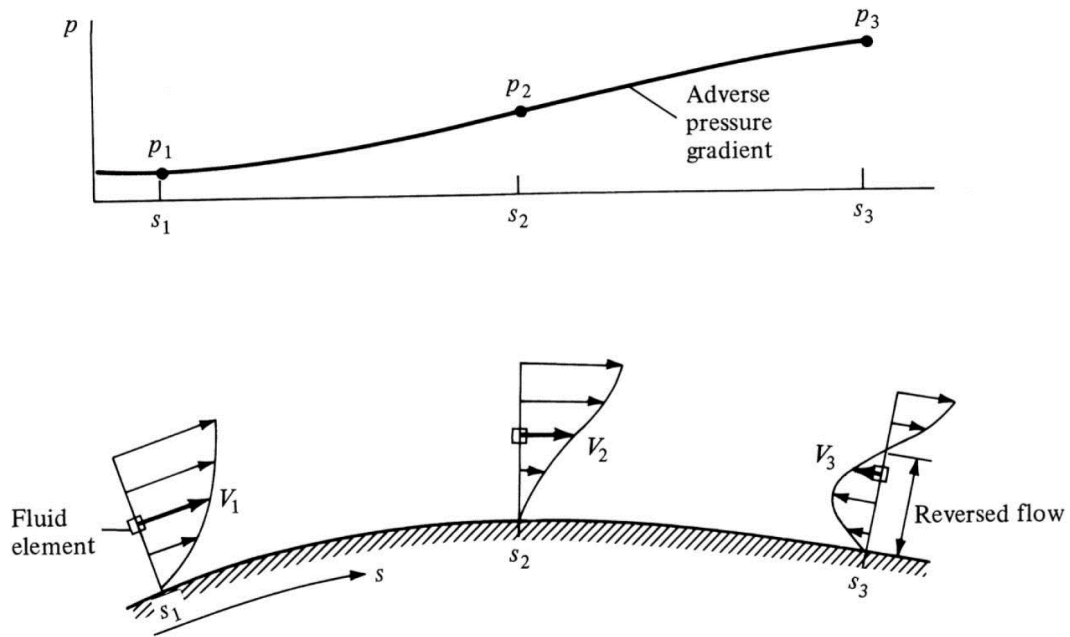


Figure 1.2 Evolution of separated flow in an adverse pressure gradient (Anderson, 2010)

Because of flow separation, the pressure distribution over the body is greatly altered. The larger wake generated by the body moving through a fluid creates a pressure difference over the body; this results in a net force over the body as well. This force manifests mainly as drag, or more specifically pressure drag. Pressure drag is one of the two main sources of drag in fluid flow, the other being drag caused by friction between a body and the fluid, or skin friction drag. Where pressure drag is the integration of pressure over a body, friction drag is the integration of

shear stress over a body. If there is a large amount of separation over a body, then pressure drag will be a major contributor to overall drag. If flow is controlled or otherwise behaves in such a way that there is little separation present, then pressure drag will be greatly reduced (Anderson, 2010)

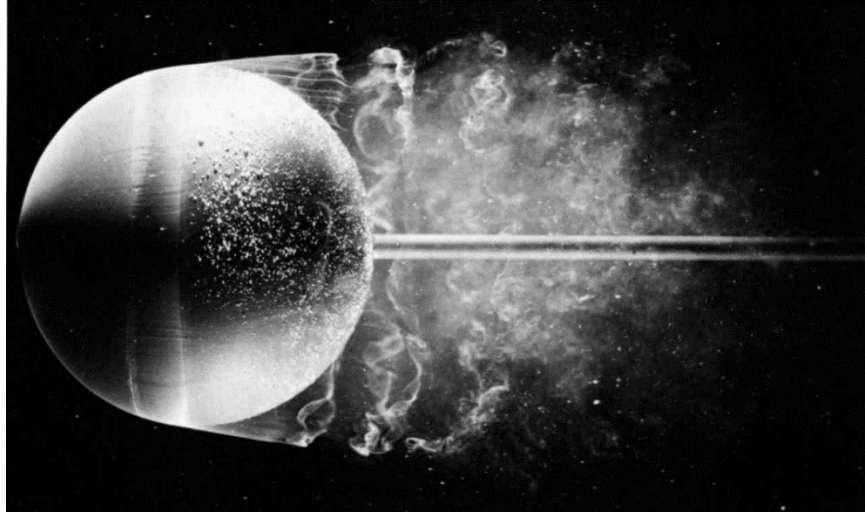


Figure 1.3 Visualization of separated flow over a sphere (van Dyke, 1982)

In general, boundary layers can exist in two states: laminar and turbulent. If flow in a boundary layer is smooth and steady in time, then it is generally considered laminar. If flow is irregular and unsteady, then it is turbulent. Each type of boundary layer has different drag characteristics. Turbulent boundary layers draw in fluid from the upper region of the boundary layer toward the surface due to the eddies and high-energy, random fluctuations that are present, inducing mixing. This results in a larger time-averaged flow velocity close to the surface and higher surface shear stress compared to a laminar boundary layer. However, the increased momentum near the wall also tends to make separation less likely in a turbulent boundary layer compared to a laminar one.

Whether a boundary layer is laminar or turbulent depends on many factors. One of the most important factors in boundary layer type is Reynolds number (Eq. 1). At Re values larger than 500,000, boundary layers usually transition to turbulent (Anderson, 2010). At standard commercial aircraft flight speeds, this critical number is reached almost immediately, meaning for the majority of circumstances the boundary layer over an aircraft is turbulent.

$$Re = \frac{\rho u x}{\mu} \quad (1)$$

Turbulence production in the boundary layer is mostly concentrated in the region very close to the wall. Klebanoff (1954) found that 80% of turbulence production occurs in the lower 20% of the boundary layer. The boundary layer itself can be broken down into several distinct regions which all have different flow characteristics (Fig. 1.4). These regions include the viscous sublayer, the buffer layer, the logarithmic region, and the wake region.

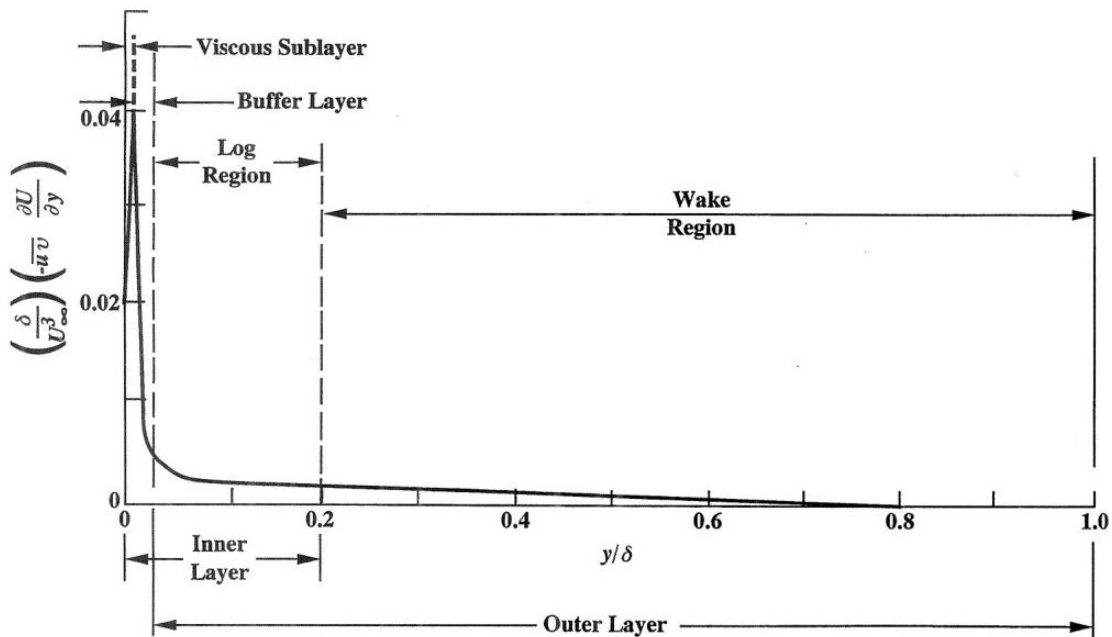


Figure 1.4 Turbulent energy production rate at different wall heights (Kline *et al*, 1976)

Because in the lower regions of the boundary layer viscous forces are much more dominant than inertial ones, it is useful to refer to time (Eq. 2) and length (Eq. 3) in viscous terms. This allows the relative size of fluid effects and mechanisms of flow control to be understood more easily.

$$t_v = \left[\frac{\partial u}{\partial y} \right]^{-1} \quad (2)$$

$$l_v = \sqrt{\nu t_v} \quad (3)$$

Also of importance is the shear stress at the wall (Eq. 4) and wall velocity scale, also called friction velocity (Eq. 5).

$$\tau_w = \mu \frac{\partial u}{\partial y} \quad (4)$$

$$u_* = \frac{l_v}{t_v} = \sqrt{\frac{\tau_w}{\rho}} \quad (5)$$

These length, time, and velocity units are known as viscous scales. Dividing viscous length scale by distance creates the dimensionless wall unit (Eq. 6). The viscous sublayer of the boundary layer consists of the region from 0 to 5 wall units, the buffer layer from 5 to 30 wall units, and the logarithmic region from 30 wall units outwards until reaching 20% of the total boundary layer height (Sreenivasan, 1987).

$$y^+ = \frac{y}{l_v} \quad (6)$$

An important factor in turbulence generation is the formation and breakdown of low-speed streaks. Near the wall, flow patterns are generally characterized as streaks of fluid moving at both relatively high and low speeds. As low-speed streaks move downstream, they begin to rise into the buffer region until suddenly undergoing a “bursting” motion that sharply lifts them farther from the wall. This burst occurs at about 10 wall units. The streaks carry their low-momentum flow through the bursting process, which is ejected into the higher-momentum logarithmic region. This low-momentum and high-momentum flow mixes and generates random turbulence oscillations. Eventually, the low-speed streak falls back to the wall and starts a new bursting cycle (Kim, 1971). A drawing of this bursting process is shown in Fig. 1.5 (Blackwelder and Eckelmann, 1978) and a visualization of a low-speed streak is shown in Fig. 1.6 (Smith *et al*, 2012).

Low-speed streaks generally occur every 100 wall units spanwise in 2D flow and are about 10 to 30 wall units in width (Kim, 1971). The streamwise distance of one burst is usually greater than 1,000 wall units in length (Blackwelder and Eckelmann, 1978). Low-speed streak growth and breakdown is part of what generates mixing and turbulence itself in the turbulent boundary layer, meaning it is responsible for a turbulent boundary layer’s tendency to stay attached. Understanding the size and behavior of low-speed streaks could be key to development of flow control; shark skin flow control methods may have direct links to low-speed streaks.

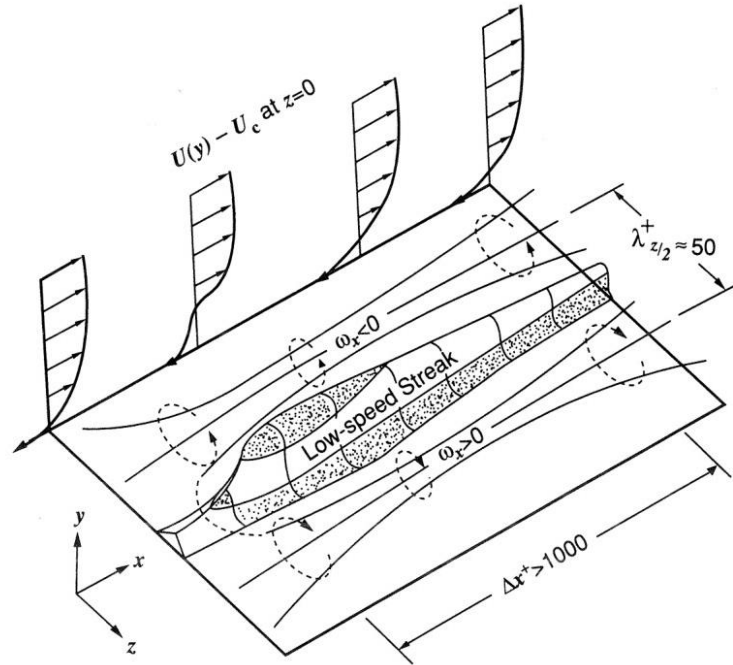


Figure 1.5 Lifting and bursting process of a low-speed streak (Blackwelder and Eckelmann, 1978)



Figure 1.6 Bubble time line visualization of low-speed streak, side view. Wire is placed $5 y^+$ from the wall, timeline generation is 30 Hz (Smith *et al*, 2012)

1.3 Mechanisms of Flow Control

As mentioned previously, there are two categories of flow control: passive and active. Passive flow control is capable of continuously altering flow conditions and requires no control system, while active flow control is tunable to specific situations but requires energy to be spent. There are multiple methods of flow control, and there is not always one way to reduce drag. Some flow control systems might focus on reducing skin friction drag while others aim to prevent separation. This section will give an overview of prominent flow control mechanisms related to this investigation, some of which are present on shark skin.

One method of reducing skin friction drag is through use of longitudinal riblets placed in the viscous sublayer. Many shark species feature riblets on their scales (Reif, 1985). As previously mentioned, the viscous sublayer of the turbulent boundary layer experiences bursts and ejections of low-speed streaks. These bursts result in spanwise crossflow along a wall, which increases shear stress. Longitudinal riblets inhibit this crossflow, resulting in a reduction in shear stress and a reduction in skin friction drag. By altering riblet protrusion height and spacing, Bechert *et al* (1997) was able to obtain a skin friction drag reduction of up to 10%.

Another passive control method caused by surface geometry is dimples on a blunt object. A sphere with dimples on it has as little as 50% of the drag a smooth sphere does in certain scenarios (Bearman, 1976). However, unlike riblets, dimples do not reduce skin friction drag but instead reduce pressure drag by controlling flow separation. Due to the geometry of a sphere, flow experiences an adverse pressure gradient as it passes over the top. Choi *et al* (2006) found that when dimples are present on the surface, each dimple creates a small separation bubble. At the top of this separation bubble, the unstable buffer layer generates an increase in turbulence (Fig. 1.7). At the end of the dimple, the turbulence adds enough momentum to the flow for it to

overcome the adverse pressure gradient. The now high-momentum flow at the surface of the sphere continues forward, past the point of separation for a comparable smooth sphere.

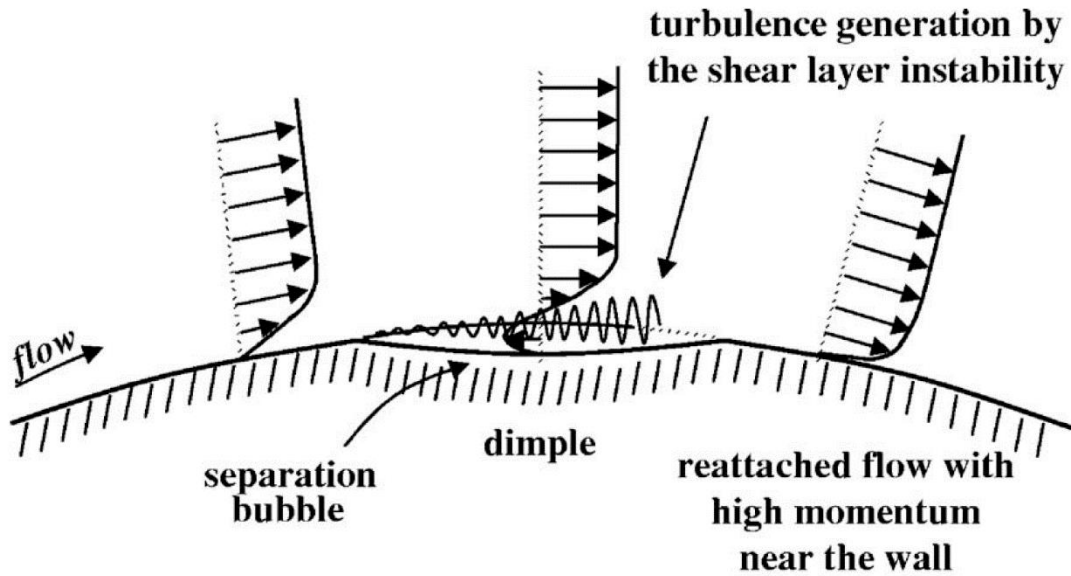


Figure 1.7 Buffer layer turbulence increase inside a dimple on a sphere (Choi *et al*, 2006)

Dimples add energy to wall flow, enabling it to overcome the adverse pressure gradient. Some active flow control techniques use the same principles. Koga (1985) used an oscillating flap to add energy to wall flow. By having the tip of the flap briefly reach into the buffer layer, the flap was able to induce mixing between the high-momentum flow in the upper regions of the boundary layer and low-momentum flow close to the wall. This reduced the size of a separated flow region behind a rear-facing step by up to 40%. Shark scales are hypothesized to act in a similar manner (Wheelus, 2015). A similar experiment by Miao (1991) used an oscillating fence on a rear-facing step to create a vortex upstream of the separation. As the frequency of oscillation increased, so did the separation reduction, showing a correlation between energy input

(moving the fence) and drag reduction (controlling separation). The maximum reduction in separation was 40%.

Instead of encouraging mixing, active flow control can add energy to the wall flow more directly. By tangentially blowing air out of an airfoil into a region of separated flow, the high-momentum air added effectively replaces the low-momentum particles. Siefert *et al* (1993) used blowing over a deflected trailing-edge flap to remove separation from the flap entirely. However, blowing is not always effective in all cases. Huang *et al* (2004) demonstrated using numerical simulation that blowing can sometimes increase lift by generating circulation while actually increasing separation and raising drag. This is an example of the downsides of active flow control: in certain situations, the use of the flow control technique may even produce additional drag and thus must work with a control system on board a vehicle to determine when the flow control should be activated.

Another method of preventing separation with active flow control is by using suction to remove low-speed flow at the wall. Suction control is a fairly mature area of study—Prandtl described the use of suction to prevent separation over a cylinder in his first presentation on the beginning of scientific flow control (1904). By removing low-speed wall flow, higher-speed flow is forced closer to the wall. Like always, this flow is less prone to separation and thus suction can reduce overall pressure drag. Studies of suction over airfoils have shown to increase lift, prevent stall, and reduce drag (Alrefi and Acharya, 1996 and Fischer *et al*, 1983). However, suction control does have some downsides, such as the need to remove larger and larger amounts of air as free-stream velocity increases and the need to carry heavy suction systems on board an aircraft.

1.4 Shark Skin Morphology and Flow Control

Shark scales contain many examples of flow control outlined in the previous section. Now that the physics behind how these flow control methods reduce drag has been explained, the specific implementation of these techniques on sharks can be discussed. Interestingly, research into shark scales began with the observation that shark scales implemented a known drag-reduction method: riblets (Bechert *et al*, 1985). This section will give an overview of a history of flow control research specifically related to sharks.

Sharks are some of the oldest animals on earth, having an evolutionary history spanning hundreds of millions of years (Martin, 2001). One species, *Isurus Oxyrinchus*, the mako shark, is of particular interest. The mako is an efficient apex predator, capable of travelling up to 55 kilometers in a single day and swimming at burst speeds of up to 20 m/s, making it the fastest species of shark on earth (Martin, 2001). All species of sharks have skin covered with millions of tiny scales, also called denticles. Mako scales are the focus for flow control due to two factors: the presence of longitudinal riblets and ability of denticles to bristle (Motta *et al*, 2012).

Shark scales are attached to the epidermis (outer layer) of shark skin. Scale shape and size depends greatly on species, as well as location on the shark's body. Mako scales are about 200 μm in height and curve backwards as they rise from the shark. Mako scales generally range from 100 to 300 μm in length and 150 to 200 μm in width. Most scales are roughly diamond-shaped and are arranged in random rows over the shark. Some scales contain longitudinal riblets while others are smooth (Motta *et al*, 2012) (Fig. 1.8).

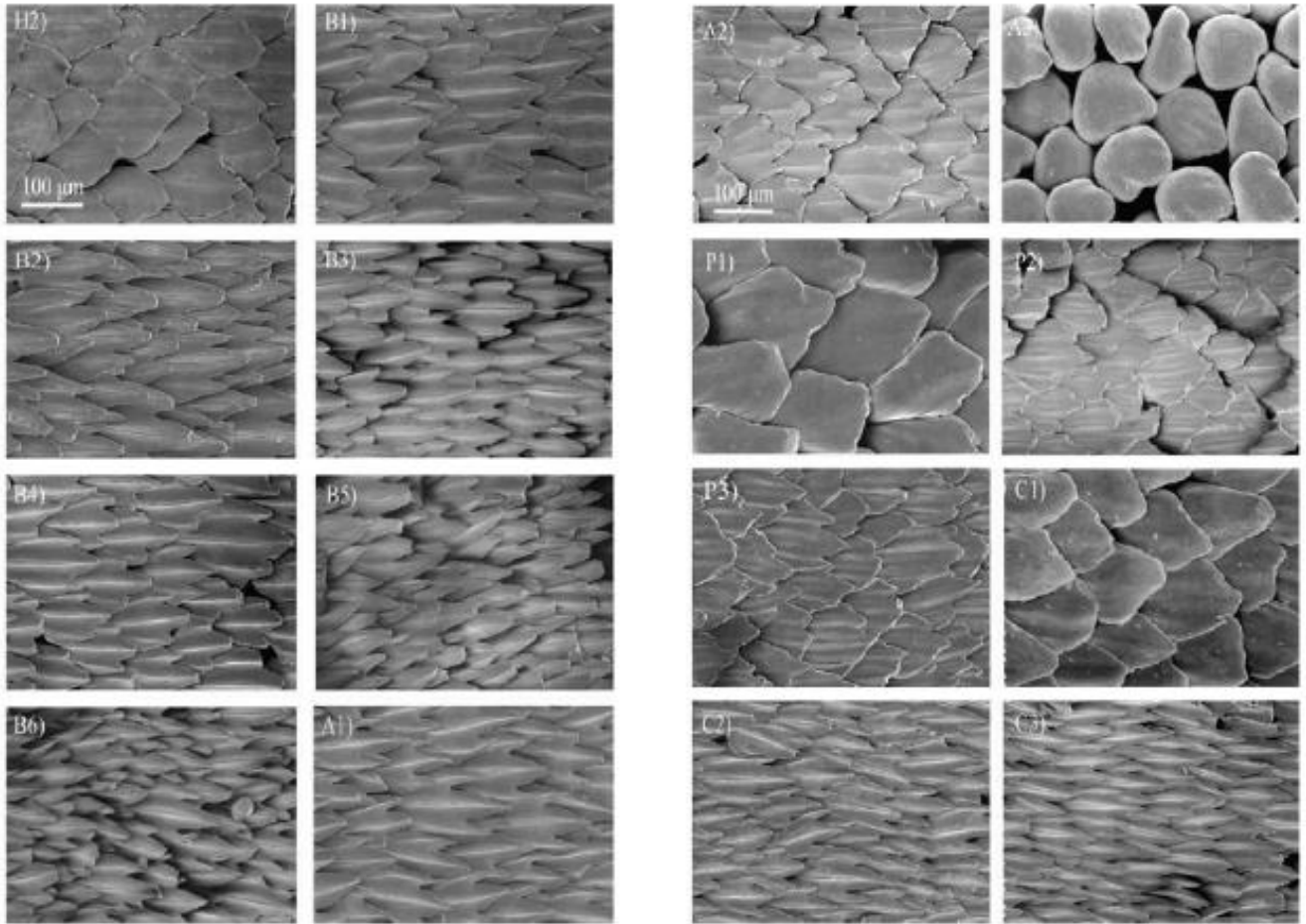


Figure 1.8 Mako scale variants at approximately 200x magnification. Scales A1-A3 are located in posterior region, B1-B6 gills region, C1-C3 tail region, and P1-P3 pectoral fin (Motta *et al*, 2012)

Some shark scales are movable and can be individually bristled (Fig. 1.9). When released, the scales relax to an angle somewhere between the maximum bristling angle and completely flat against the shark's body. This resting angle varies with location over the shark—the most flexible locations are along the side of the shark's body, with the highest angle being directly behind the gills (Motta *et al*, 2012) (Fig. 1.10). Because the gills are the widest point of the shark, flow over them experiences an adverse pressure gradient and make the gills a prominent location for the formation of reverse flow.

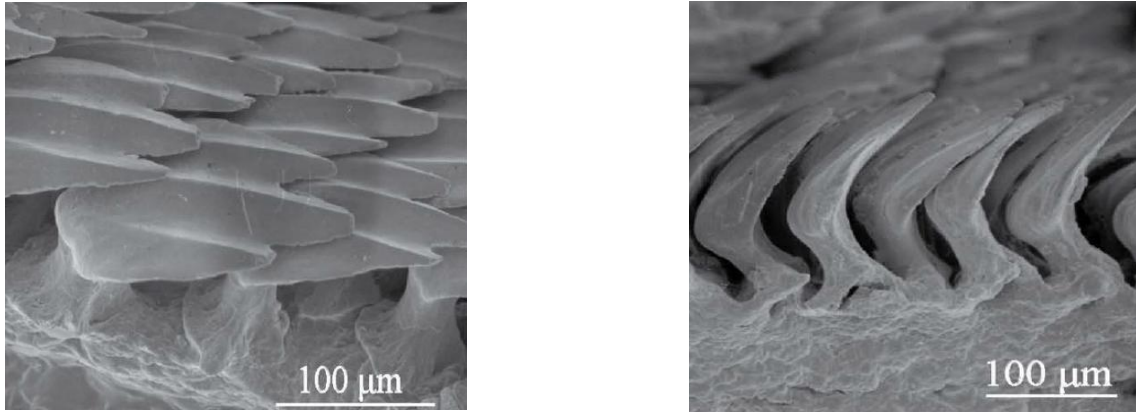


Figure 1.9 Scanning electron microscope image of mako scales. Left image is resting position; right image has been manually bristled (Lang *et al*, 2014)

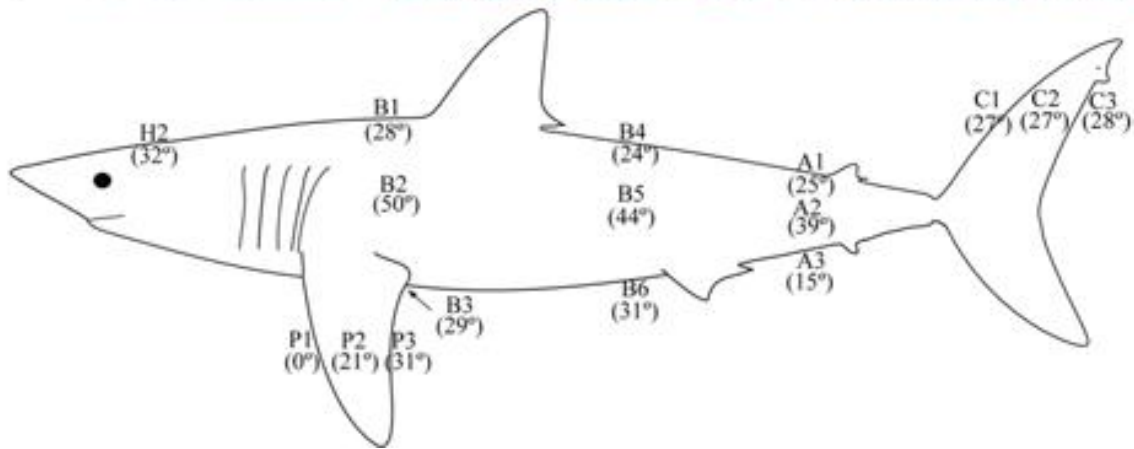


Figure 1.10 Average maximum bristling angle of mako scales (Lang *et al*, 2011)

Research on shark skin in relation to flow control started in 1985. Bechert recognized a link between riblets as a method of skin friction reduction and the riblet structures located on shark skin (1985). One test of riblet structures based on shark skin geometry showed a possible reduction in skin friction drag to be as high as 10% (2000). Bechert also tested vast arrays of artificially created scales that were capable of being bristled to various angles. However, tests did not show a noteworthy improvement in skin friction reduction with bristled scales; in fact, a two-dimensional array of ribs outperformed the bristled scales at reducing skin friction drag (1997).

Bechert theorized that bristled scales could possibly act as vortex generators (1985) but did not investigate this idea any further.

Early research on shark skin flow control focused on skin friction drag reduction; it would be almost 10 years before the idea of separation control by scales was studied. While bristled scales appeared to have little effect on skin friction reduction, they play an extremely important part in separation control. Lang *et al* (2008) theorized that an array of bristled scales could act as a rough surface to provide separation control. As scales bristle, the cavities formed between bristled scales would act like dimples on a sphere, reducing separation and thus reducing pressure drag. Using enlarged, fixed models of scales placed in a water tunnel, Lang demonstrated that vortices formed in the cavities created between scales when bristled, with the riblets appearing to promote vortex formation. Lang studied the possibility of the mako shark actively pressurizing its body to bristle scales. However, subjecting mako skin to high subcutaneous pressure did not result in a significant change in scale angle (Lang *et al*, 2008).

Further investigating the flow mechanics of bristled scales, Wheelus (2015) constructed a fixed bristled scale array closely resembling the relaxing angle of mako scales (45°). Using PIV, Wheelus observed mixing between cavities and the free stream, signifying the possibility that high-speed flow is drawn close to the wall by the bristled scales to control separation (Fig 1.11).

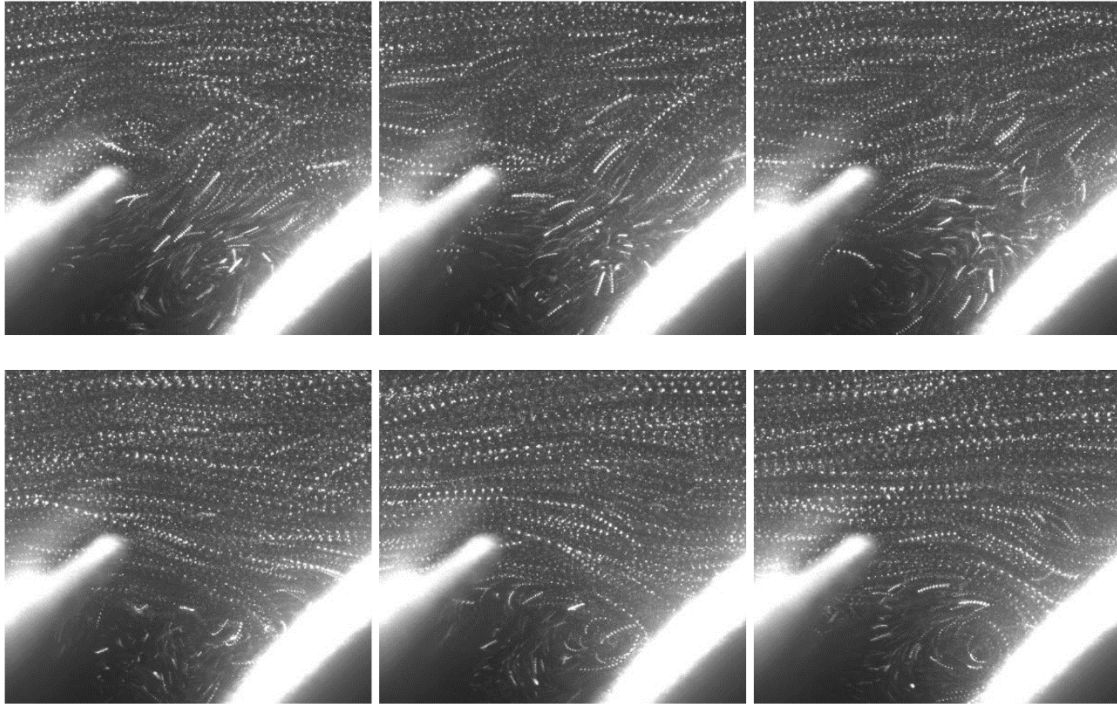


Figure 1.11 Particle ejection from cavity into the boundary layer at 0.38 m/s. Each row is a separate sequence from left to right (Wheelus, 2015)

The bristled scale array studied by Wheelus behaved similarly to square cavities studied by Djendi. As the boundary layer flow passed over the square cavities, it mixed with vortices inside these cavities. This inflow and outflow process seemed to be linked to the formation of low-speed streaks (Djendi, 1998), which are a sign of flow reversal (Hammerton and Lang, 2015). Based on the height of bristled mako scales, Wheelus theorized that mako scales would be just large enough to protrude into the buffer layer. If scales bristled in the presence of low-speed streaks, they would initiate mixing between the different regions of boundary layer flow to postpone separation (Wheelus, 2015). Mako scales are approximately the width of a low-speed streak, about 10 to 30 viscous length scales.

Wheelus also studied the possibility that sharks scales could be passively actuated by reversing flow. By using a small water jet, it was found that mako scales could be bristled by

water (Fig. 1.12). The flow speeds necessary to bristle a single scale (1-3 m/s) were found to be within the realm of reversed flow velocities of typical mako swimming speeds (20-30% of 6-34 m/s) (Wheelus, 2015). This indicates the possibility that shark skin may act as a flow-actuated, passive separation control method.

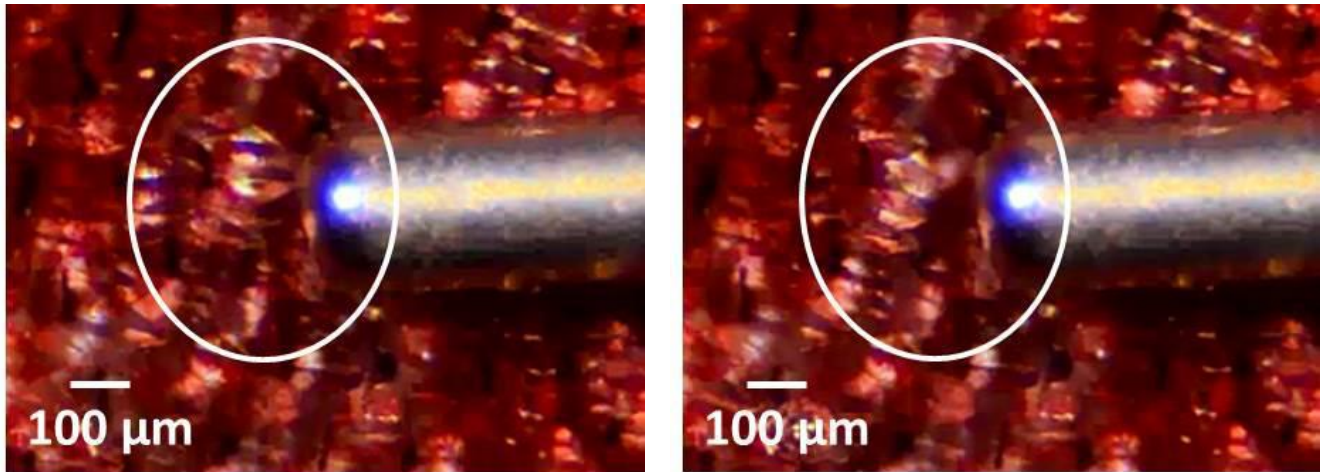


Figure 1.12 Actuation of a single scale due to water jet. Scale is unbristled on left and fully bristled on right (Wheelus, 2015)

After studying flow properties of bristled scales and testing the possibility of flow actuation, the flow control capabilities of shark skin were tested (Lang *et al*, 2014). Samples of adult mako skin from the flank region, where scales are most flexible, were mounted on a hydrofoil at angles of attack high enough to generate separated flow. Using DPIV, Lang found that a hydrofoil with shark skin attached to it experienced a significant reduction in reversed flow compared to a smooth one (Fig. 1.13). As mako scales are microscopic in size, scale bristling was unable to be observed during this test.

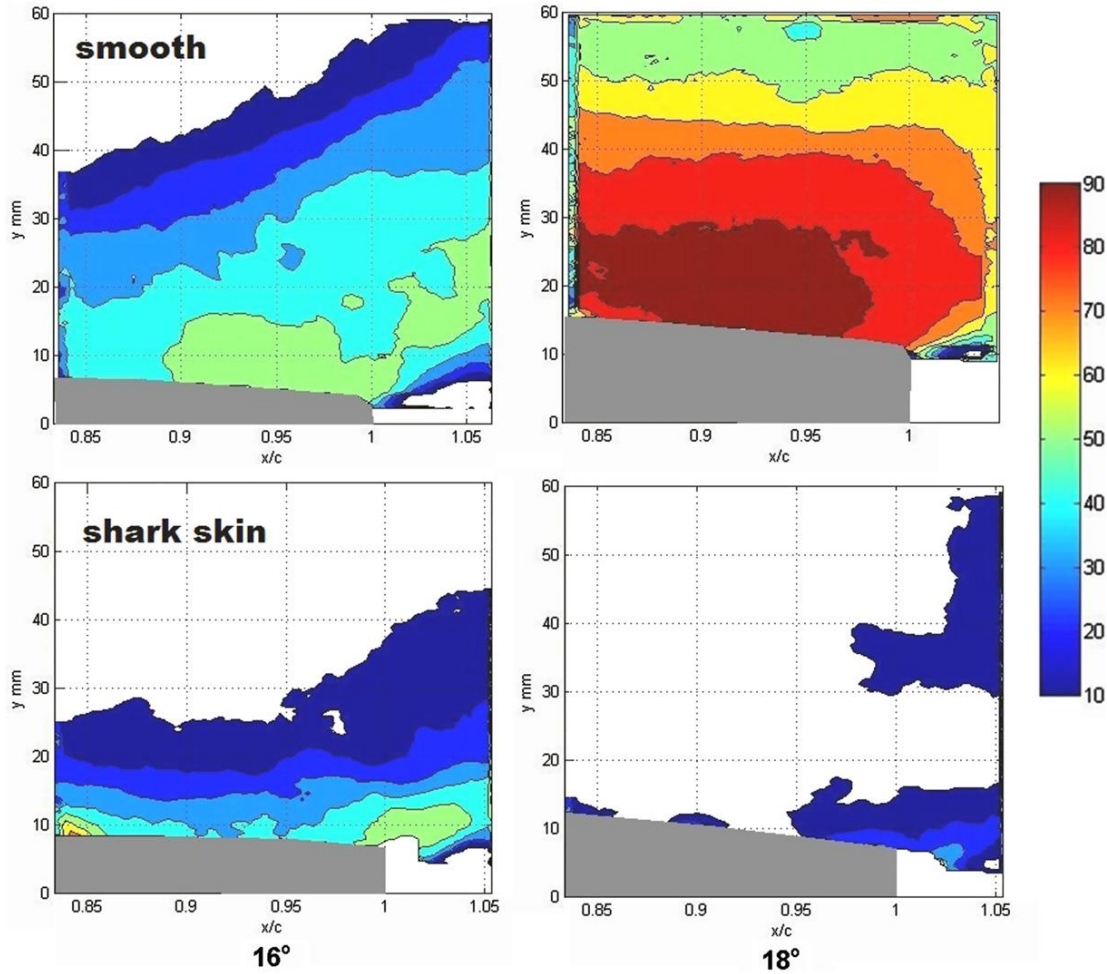


Figure 1.13 Time-averaged backflow coefficient color contour over smooth and shark skin-covered hydrofoils at 0.32 m/s (Lang *et al*, 2014)

Lang conducted future tests on shark-skin covered hydrofoils, painting over the shark skin to prevent scales from being bristled. When scales were painted over, they did not provide any significant separation control (Lang *et al*, 2014).

Additional testing by Devey and Hancock (2016) placed shark skin on an airfoil and used a load cell to measure drag force and pressure taps to measure surface pressures. This testing did not show any significant difference in drag force or surface pressure distribution between a clean airfoil, an airfoil with shark skin attached, and an airfoil with shark skin attached but painted over. Further testing using an air jet on shark skin showed that scales do not begin to bristle in air

until reversed flow speeds of approximately 60 m/s, far beyond expected reversed flow velocities in the previous wind tunnel test. Shark skin quickly dries out and becomes brittle when exposed to air, which impairs its ability to bristle. To remedy this issue, the scales were kept constantly wet in the experiment, but the surface tension of the water is also believed to prevent the scales from bristling. These studies suggested that shark skin is not practical for studies of separation control in airflow.

1.5 Summary and Objectives

It has been demonstrated that mako scales are capable of being bristled by reversed flow and that shark skin can reduce separation and potentially pressure drag. Bristled scales protrude about 5% into the boundary layer on a shark. At this size, they interact directly with the buffer layer, and when bristled both inhibit further flow reversal near the wall and encourage mixing between low-momentum wall flow and higher-momentum flow in the upper regions of the boundary layer. The width of mako scales also corresponds to the size of a low-speed streak, approximately 10 to 30 viscous length scales.

Shark scales appear to act as a passive flow control mechanism that is flow-actuated, only activated when necessary and possibly triggered by reversing flow inside low-speed streaks. The link to the low-speed streaks is of particular interest: low-speed streaks are linked to the *beginning* of flow reversal, not a sign that it has already occurred (Hammerton and Lang, 2015). By reacting to low-speed streaks, shark scales could anticipate the production of reversed flow and activate to control separation. A flow control system based on shark skin could combine the benefits of passive and active flow control. This method of flow control would require no control

system to determine when to activate it but would only engage when needed to control separation.

Mako skin is effective at reducing separation in water; however, the benefits are not immediately able to be replicated in airflow. Even though shark skin does not reduce separation in air, the hypothesized mechanisms for flow control (vortex generation through cavity flow to encourage momentum exchange) should be applicable in airflow. For further study of shark skin's separation-reducing effects in airflow, a mechanical model similar to shark scales must be created. Shark skin is capable of flow control at free-stream speeds of about 0.5 m/s, with a dynamic pressure of 125 Pa (Wheelus, 2015). This dynamic pressure corresponds to roughly 14.6 m/s in airflow, suggesting airflow should be able to actuate a shark scale model.

If a mechanical model of shark skin is capable of being actuated by reversed airflow, then it may replicate the separation control abilities of shark skin. First, the theorized method of flow control—actuation of scales by reversed flow—must be confirmed. The objective of this research is to design, produce, and test various small microflaps modeled after shark scales. The microflaps will be created in 2D (modeled after rectangular flaps) and 3D (modeled after mako shark scales) variants.

The microflaps will be placed in a low-speed wind tunnel in various configurations and flow conditions. Due to their larger size compared to shark scales, the microflaps can be easily observed to bristle and fluctuate. The focus of the experiments performed in this thesis is to understand the conditions that will cause microflaps to actuate, not the potential separation control ability of microflaps. The boundary layer flow velocities and conditions necessary for microflaps to be actuated by the flow will be quantified. Various devices will be used to create different reversed flow conditions, such as fences and diffusers.

Shark scales have a long history of research into their flow control effects in water. Although fluid properties of water and air are different, an array of scales sized to the lower 5% of the boundary layer may be capable of reducing separation in airflow. Demonstrating that low-momentum flow can actuate microflaps will help to confirm the method of separation control in water and be a first step towards achieving separation control in airflow. The implementation of this passive, flow-actuated control mechanism could result in drag reduction for all vehicles.

CHAPTER 2: SHARK SKIN MODEL DESIGN AND EXPERIMENTAL SETUP

This section explains the facilities utilized to conduct the tests as well as the design process of a mechanical model of shark scales, called microflaps. Various sets of microflaps, based on shark scale geometry, were 3D printed and placed in the boundary layer of a low-speed wind tunnel. After studying the test conditions in the University of Alabama low-speed wind tunnel, microflaps were sized to correspond with the lower 5% of the boundary layer.

2.1 Experimental Facilities

Experiments were performed in the University of Alabama boundary layer wind tunnel in 135 Hardaway Hall. The tunnel is an open-circuit, blowing design, consisting of an 8.5:1 contraction to a 4.87 m test section with cross-sectional dimensions of 0.914 m by 0.304 m. The boundary layer tunnel is equipped with a moveable ceiling for the creation of different pressure gradients. Test speeds are possible from 1.2 to 50 m/s, and the test section has optical access on the walls and floor. Free-stream turbulence levels are 0.7% at 10 m/s, 0.45% at 20 m/s, and 0.39% at 30 m/s, measured 3.91 m downstream from the start of the test section. The tunnel can accommodate various measurement devices, including thermocouples, digital barometers, linear traverse systems, hot film probes, and more. A schematic of the wind tunnel design is shown in

Fig. 2.1. For all tests performed, the movable ceiling was flat to ensure a constant cross-sectional area in the test section.

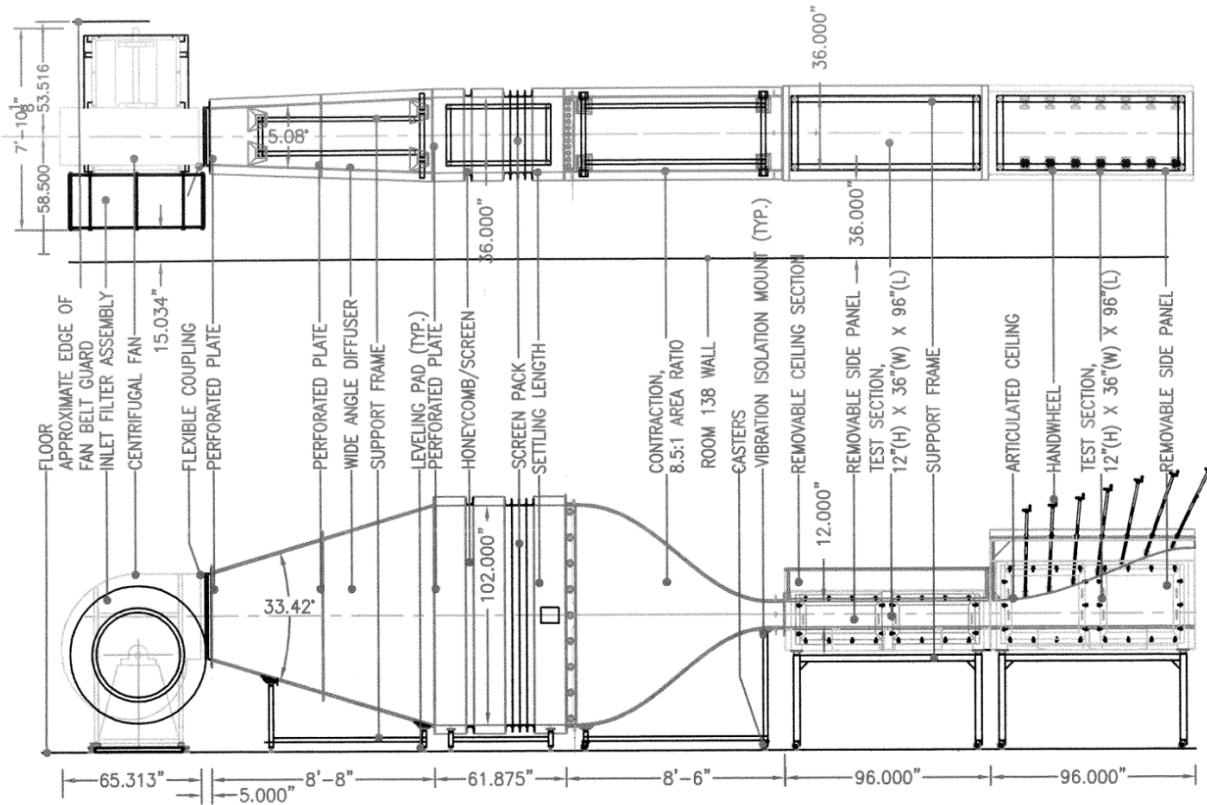


Figure 2.1 Schematic of wind tunnel layout

Tunnel speed was recorded using a pitot-static probe at the entrance of the test section. Pressure ports along the floor of the entire test section allowed for static pressure measurements throughout the test section. Pressure was measured using a PSI-9116 pressure scanner (± 2.48 kPa $\pm 0.05\%$). Air density was calculated using the ideal gas equation (Eq. 7). Atmospheric pressure was measured by a Druck DPI-142 digital barometer (75-115 kPa $\pm 0.01\%$) and temperature was acquired from a K-type thermocouple connected to a National Instruments USB-9211 DAQ device (0.6 °C accuracy) (National Instruments Corporation, 2007).

$$\rho = \frac{P}{RT} \quad (7)$$

To obtain velocity profiles, a boundary layer (BL) pitot probe was mounted on a Velmex XN10-0120-E25-21 linear slide. This linear traverse is 30.48 cm long and capable of movements as precise as 0.635 mm (Fig. 2.2 and 2.3).

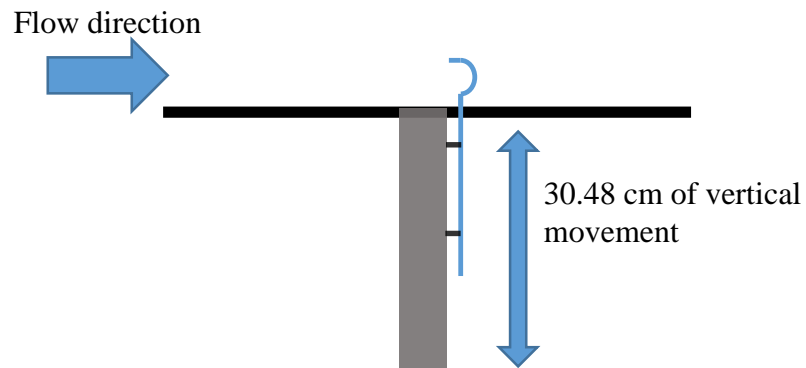


Figure 2.2 Schematic of boundary layer probe and linear traverse

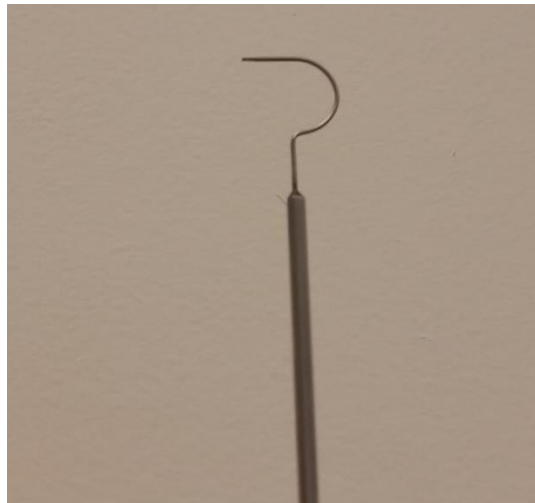


Figure 2.3 Boundary layer probe

To determine the height of the boundary layer along the test section, the pitot probe was mounted at the center of three different floor panels along the test section: panels 1, 5, and 8 (Fig. 2.4). The center of panel 1 corresponded to 0.3 m from the start of the test section, panel 5 2.73 m, and panel 8 4.5 m.

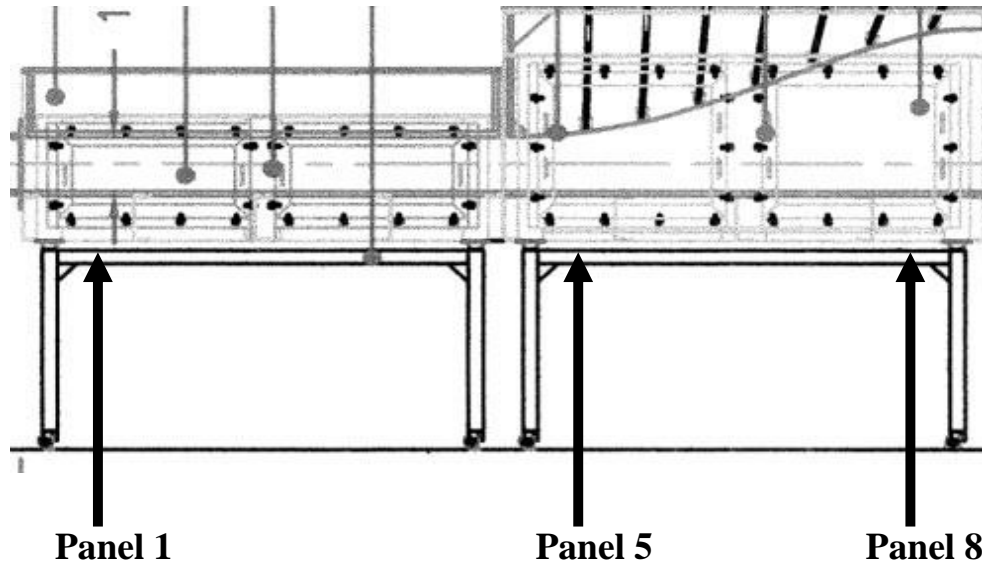


Figure 2.4 Locations of BL probe tests. Adjustable ceiling was set to flat for all tests, resulting in constant cross-sectional area for test section

The probe was placed at the floor of the wind tunnel and raised by 0.5 mm. Using the PSI-9116 pressure scanner and LabVIEW, 20 pressure measurements were obtained over a 20 second period. These 20 measurements were averaged to provide a mean pressure reading at this height. The probe was raised and measurements were repeated until the stagnation pressure measured by the probe no longer changed. Static pressures along the tunnel were measured using intermittent pressure ports in the tunnel floor. Each location was tested at tunnel speeds of 15, 30, and 45 m/s.

Using the stagnation pressure, static pressure, and air density, the local velocity was calculated for each test location and test speed (Eq. 8).

$$u^2 = \frac{2(P_0 - P)}{\rho} \quad (8)$$

The velocity profiles for each test location are shown in Fig. 2.5-2.7. Note that at test locations downstream of the test section entrance, local free-stream velocity increases due to the boundary layer displacement thickness. Total boundary layer thickness was considered where boundary layer velocity reached 99% of the local free-stream velocity. A nondimensionalized graph of boundary layer thickness versus velocity is shown in Fig. 2.8, using data obtained at panel 8 and 15 m/s free-stream velocity.

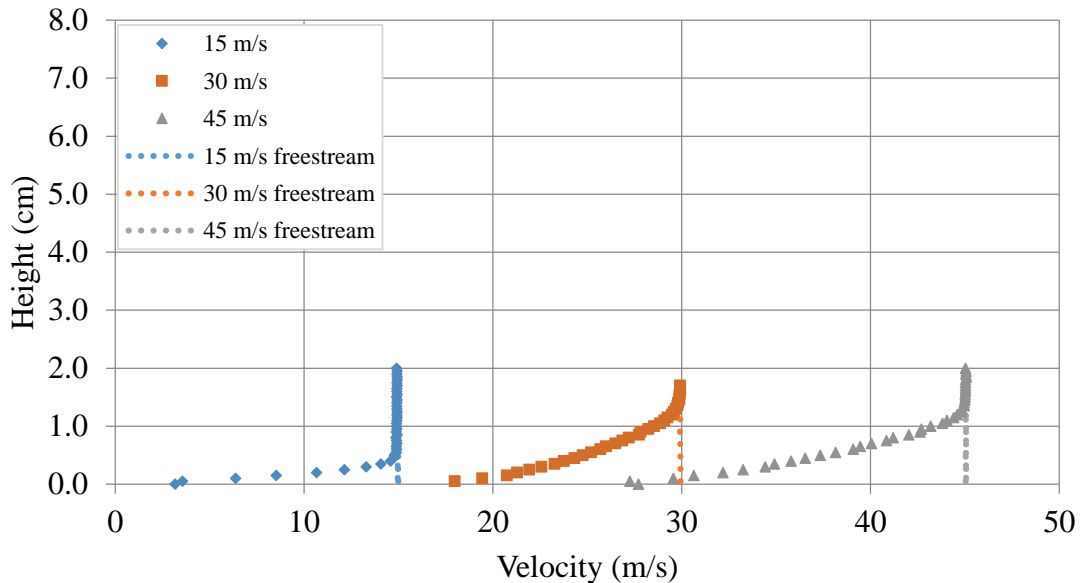


Figure 2.5 Velocity distributions in boundary layer, panel 1

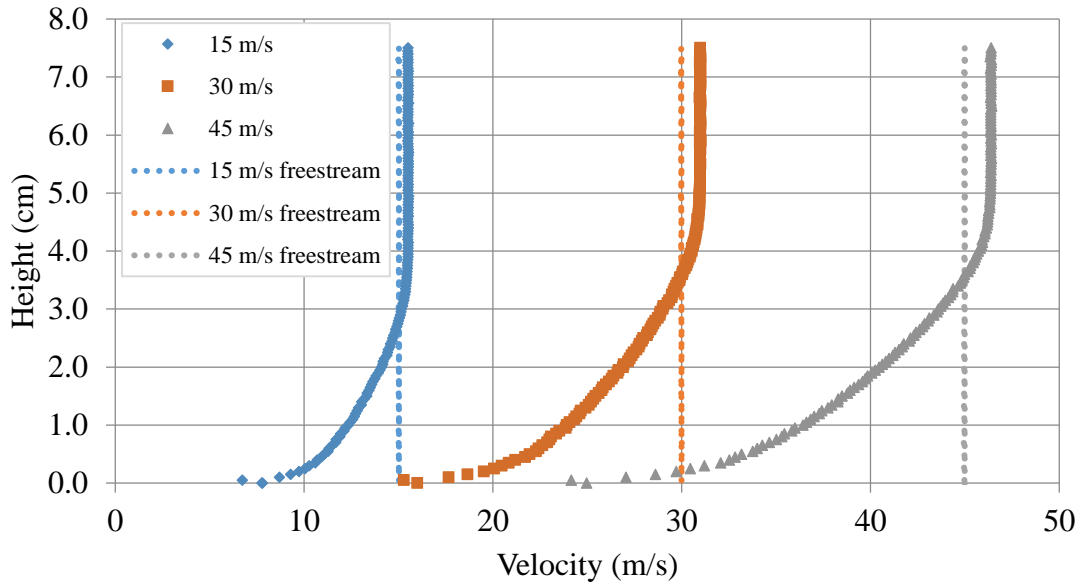


Figure 2.6 Velocity distributions in boundary layer, panel 5

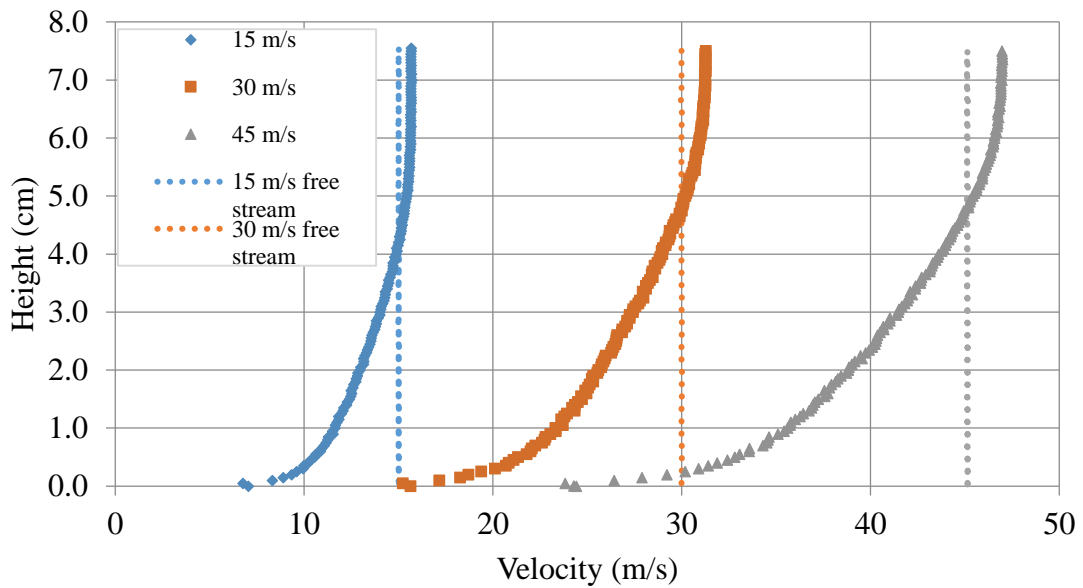


Figure 2.7 Velocity distributions in boundary layer, panel 8

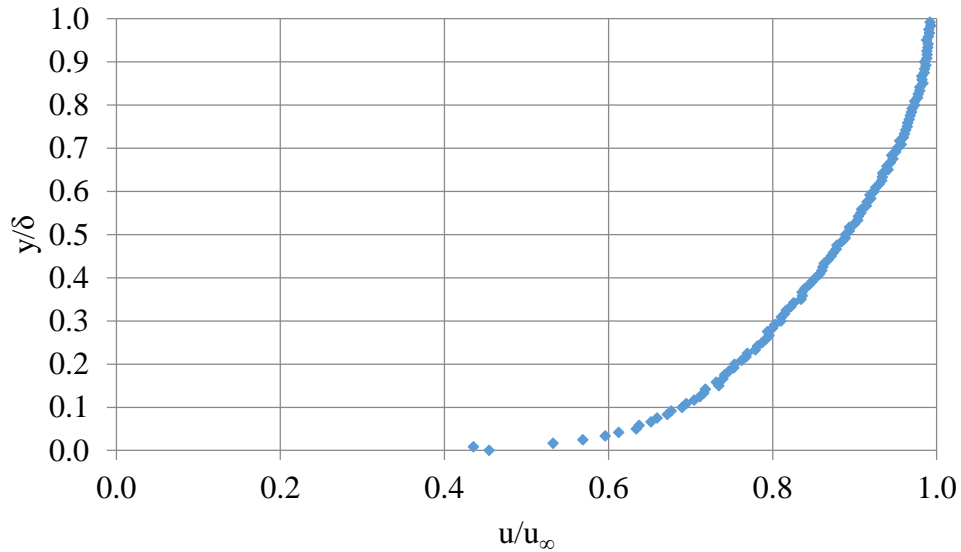


Figure 2.8 Nondimensionalized velocity distribution in boundary layer, panel 8 at 15 m/s

Static pressure measurements were acquired along the floor of the test section at each speed and converted to pressure coefficient (Eq. 9). Free-stream stagnation pressure was acquired from a pitot-static probe at the start of the test section.

$$C_p = \frac{P - P_{0_{fs}}}{\frac{1}{2} \rho u_{\infty}^2} \quad (9)$$

At panel 8, static pressure ports had larger standard deviations than the rest of the test section and were observed to fluctuate during testing (Fig. 2.9). This was possibly due to interaction between the end of the test section and the standing air in the room. To avoid these fluctuations, the center of panel 7 (3.91 m downstream from the start of the test section) was chosen as the test location for the microflaps. Pressure coefficient was observed to decrease over the length of the test

section. This is caused by the growth in boundary layer height and resulting speed increase farther from the start of the test section.

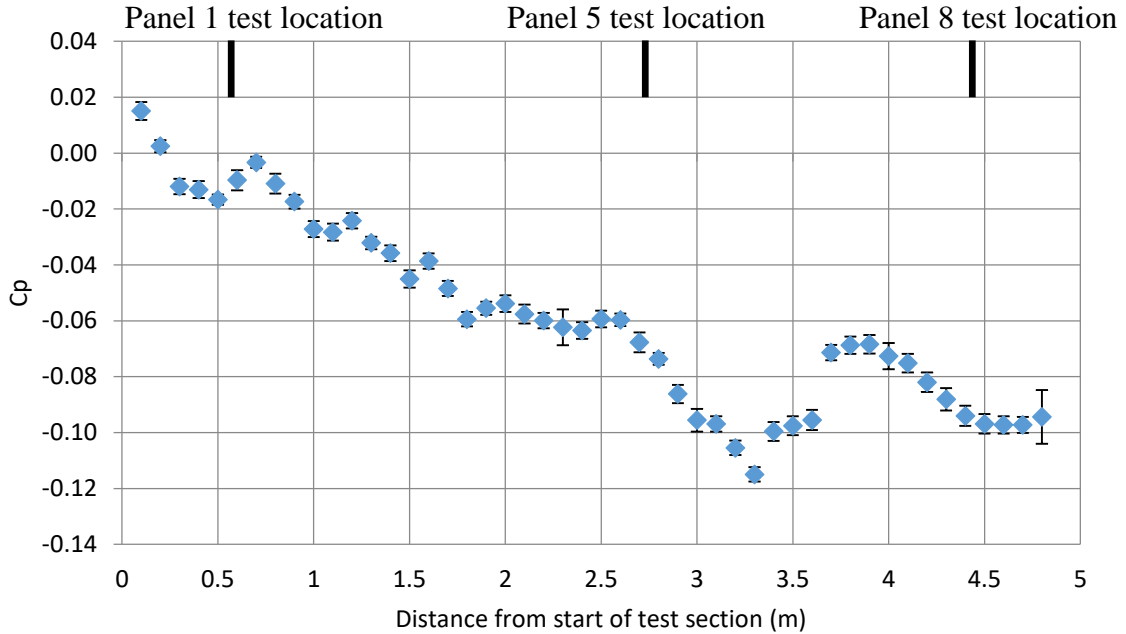


Figure 2.9 Pressure coefficient measurements along test section at 30 m/s, with standard deviation error bars

At 15 m/s, Reynolds number versus streamwise distance is approximately $9.6 \times 10^5 \frac{1}{m}$. The boundary layer in the test section was estimated to transition to turbulent after a streamwise distance of about 0.5 m. Using a fifth order Blasius approximation of turbulent boundary layer thicknesses (Eq. 10), 5% boundary layer height at panel 7 was calculated to be 3.5 mm. Fig. 2.10 shows the boundary layer height at the three locations tested as well as the 5th order Blasius approximation of boundary layer height.

$$\delta = \frac{0.37x}{\sqrt[5]{Re_x}} \quad (10)$$

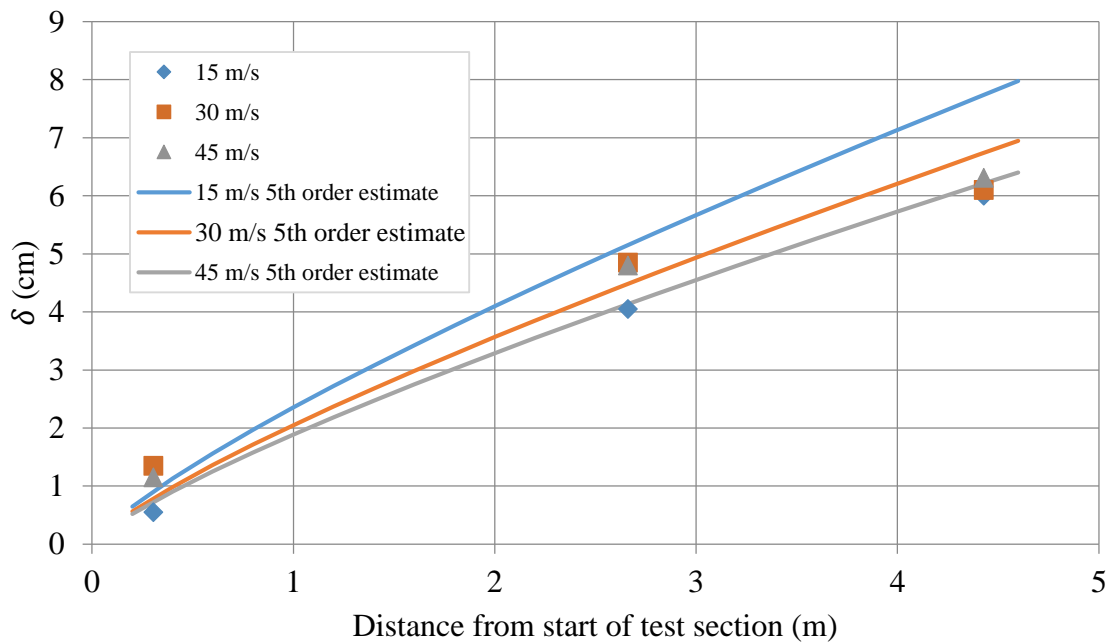


Figure 2.10 Measured boundary layer height and 5th order estimation

Using velocity profiles measured at panel 8, the wall shear stress and viscous length scales were calculated for various speeds. For 15, 30, and 45 m/s, the viscous length scale was found to be 70.5, 63.7, and 54.8 μm , respectively. Estimating the width of a low-speed streak as 30 viscous length scales, streak widths were 3.52, 3.18, and 2.74 mm, respectively.

2.2 Microflap Design Process

To test the flow control capabilities of shark scale-like objects in airflow, a mechanical model must be used. Several different versions of microflaps were designed and manufactured using a 3D printer. These microflaps were used to test whether low-momentum flow in the boundary layer is capable of actuating these scale-like objects.

The microflaps were based on the geometry flank scales of the mako shark (Fig. 2.11) which have controlled separation in water tunnel studies (Lang *et al*, 2014). Motta (2012) had identified the dimensions of individual scales (such as scale thickness, bristling angle, and scale height above the skin), which were replicated to create a scalable cross-section. Based on the boundary layer thickness measurements at the test location for the microflaps, the chord length was adjusted so the microflaps protruded 5% into the boundary layer once fully bristled.

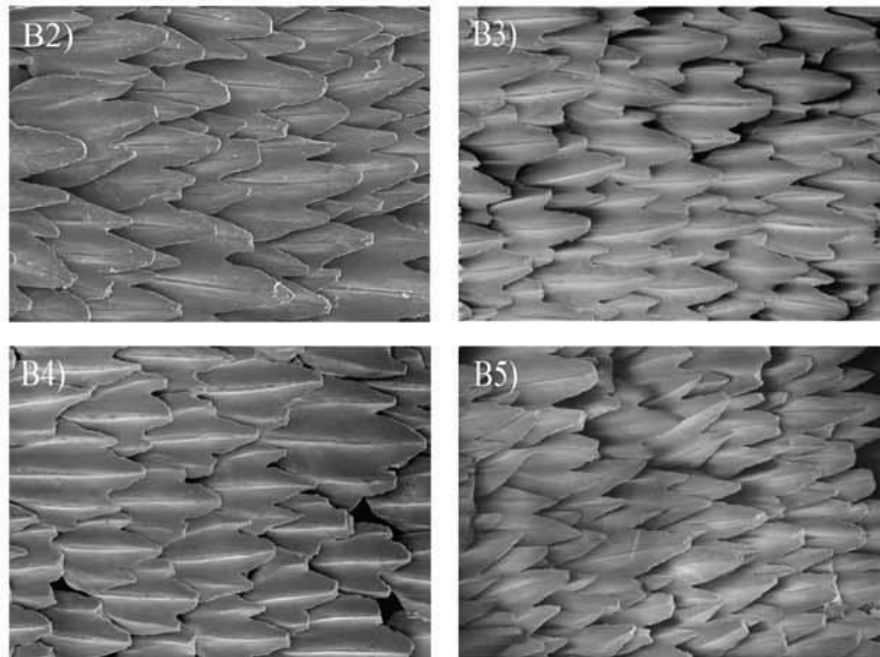


Figure 2.11 Array of scales located on the flank region of the mako shark (Motta *et al*, 2012)

Microflaps were designed in both 2D and 3D variants. 2D microflaps were designed first to test whether reversing flow could bristle a simple flap with a high aspect ratio. The 2D microflaps have a chord length of 0.5 cm and span of 10.8 cm, resulting in an aspect ratio of 21.6 (Fig. 2.12 A and Fig. 2.12 B). The microflaps included a hinge that is able to rotate along a separate axle, 0.08 cm in diameter. The hinge and axle were located in a basin below the surface

of the test section so that the base of the flap itself was even with the surface of the test section. A vertical stem protrudes from this hinge to raise the chord of the microflap to the surface of the test section. A foot was attached to the hinge opposite the flap section. This foot comes in contact with the bottom of this basin, preventing the microflap from rotating past 60° , about the maximum bristling angle of the shark scales (Fig. 2.12 C and Fig. 2.12 D). The 2D microflaps were designed both with and without longitudinal riblets to test whether riblets affected bristling. Riblets were 3.8 mm wide, 1.7 mm in height, and spaced every 9 mm in the spanwise direction. To minimize the effect of gravity on the microflap rotation, the center of gravity was placed over the pivot point.

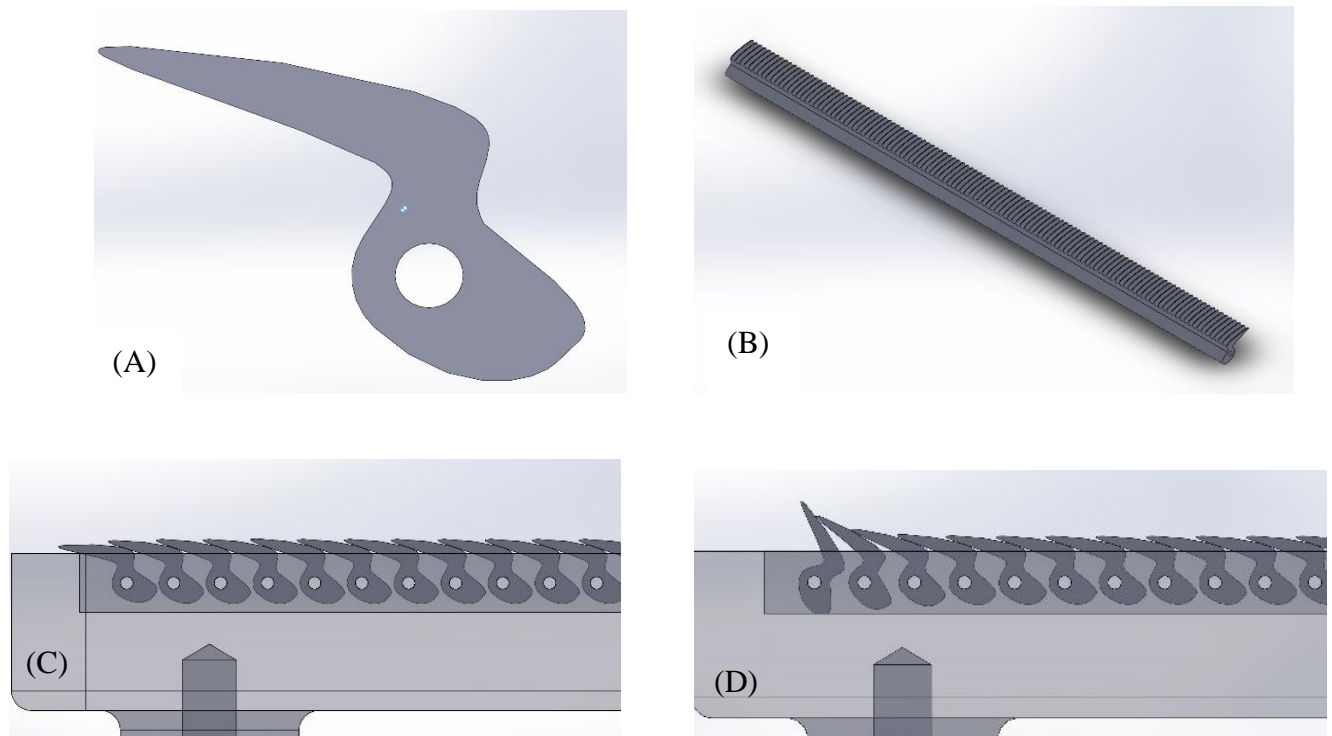


Figure 2.12 Side view of 2D microflap model with CG (A), isometric view of 2D microflap model with longitudinal riblets (B), 2D microflap model array at rest (C), 2D microflap array model showing rotation, (D)

Following testing of the 2D microflaps, 3D microflaps were designed. Each 3D microflap was based on the entire shape of a single mako flank scale rather than just a cross-section. The 3D microflaps were designed to mirror shark scale geometry as closely as possible, complete with longitudinal riblets, a serrated trailing edge, and a vertical stem protruding from the hinge (Fig. 2.13). All dimensions, such as chord length, width, and riblet spacing, were based on mako shark scale measurements obtained by Motta *et al* (2012) (Fig. 2.14).

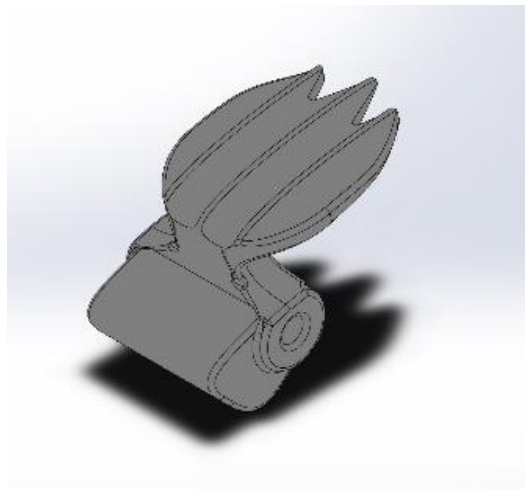


Figure 2.13 CAD model of 3D microflap design

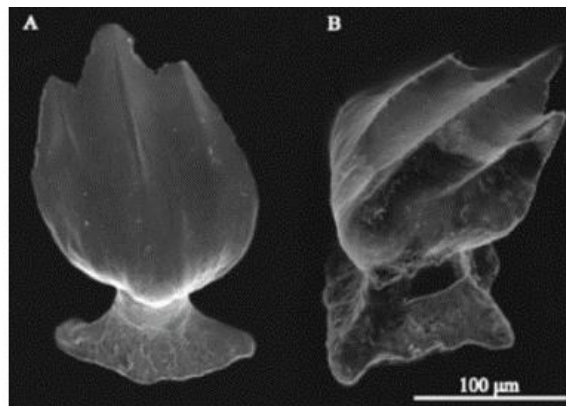


Figure 2.14 Scanning electron microscope images of individual mako flank scales (Lang *et al*, 2011)

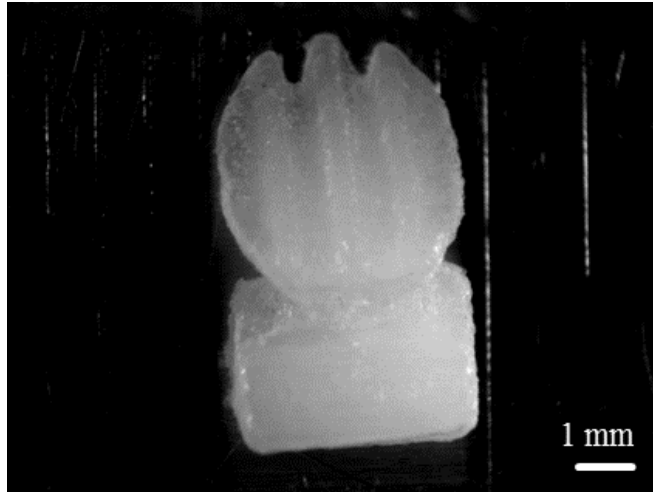


Figure 2.15 Magnification of printed 3D microflap.

The 3D microflaps have a chord length of 0.487 cm, span width of 0.375 cm, and are raised 0.188 cm from their axis of rotation by a vertical stem. Each 3D microflap has three 3.8 mm tall longitudinal riblets at 0.09 cm spanwise intervals. The final 3D microflap design protrudes only 5% into the boundary layer when fully bristled at an angle of 60° . As previously mentioned, the width of a low-speed streak was estimated as 30 viscous length scales. This made the low-speed streak widths at 15, 30, and 45 m/s 3.52, 3.18, and 2.74 mm, respectively. The 3D microflaps have a span of 3.75 mm, making them close to the width of a low-speed streak.

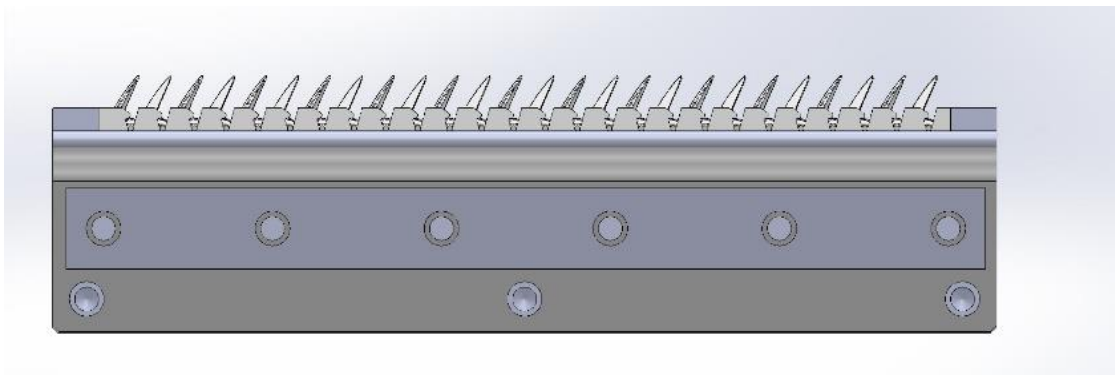


Figure 2.16 CAD model of pre-bristled 3D microflap array

All microflaps were manufactured using an Objet30 Pro 3D printer. The 3D microflaps were printed with the VeroClear material and the 2D microflaps were printed with the VeroWhite material. Material properties are shown in Table 1. Manufacturing tolerance of the Object30 Pro was 0.1 mm. After being manufactured, the microflaps were cleaned using a sodium hydroxide solution and manual abrasion to remove material left over from the manufacturing process. Twelve rows of 2D microflaps were mounted on brass axles (Fig. 2.17).



Figure 2.17 Completed array of 2D microflaps

The 3D microflaps were threaded onto the tensioned wire arrays, with 26 rows and 22 microflaps per row. For both the 2D and 3D microflaps, rows were spaced 0.3 cm apart from each other, based on spacing of real shark scale rows (Motta *et al*, 2012). Each row of 3D microflaps was also offset spanwise by one half of one scale width to ensure that each 3D

microflap overlapped the space between 3D microflaps on the row behind it, similar to shark skin (Fig 2.18).



Figure 2.18 Completed array of 3D microflaps

Table 1. Physical properties of 3D printing material VeroClear

	ASTM	UNITS	METRIC	UNITS	IMPERIAL
Tensile strength	D-638-03	MPa	50-65	psi	7250-9450
Elongation at break	D-638-05	%	10-25	%	10-25
Modulus of elasticity	D-638-04	MPa	2000-3000	psi	290,000-435,000
Flexural Strength	D-790-03	MPa	75-110	psi	11000-16000
Flexural Modulus	D-790-04	MPa	2200-3200	psi	320,000-465,000
HDT, °C @ 0.45MPa	D-648-06	°C	45-50	°F	113-122
HDT, °C @ 1.82MPa	D-648-07	°C	45-50	°F	113-122
Izod Notched Impact	D-256-06	J/m	20-30	ft lb/inch	0.375-0.562
Water Absorption	D-570-98 24hr	%	1.1-1.5	%	1.1-1.5
Tg	DMA, E»	°C	52-54	°F	126-129
Shore Hardness (D)	Scale D	Scale D	83-86	Scale D	83-86
Rockwell Hardness	Scale M	Scale M	73-76	Scale M	73-76
Polymerized density	ASTM D792	g/cm ³	1.18-1.19		
Ash content	USP281	%	0.02-0.06	%	0.02-0.06

2.3 Flat Plate Diffuser to Induce Separation

Microflaps were designed to be tested in a separated flow region. Due to the interactions of shark scales with the lower regions of the boundary layer, a method of separated flow generation that preserved the boundary layer in the test section was desired. For the creation of this separated flow region, a flat plate diffuser was designed.

Previous research into separated flow regions has often used special wind tunnel test sections to induce separated flow. Mohammed-Taifour (2015) and Patrick (1987) both used a diverging-converging floor in a wind tunnel to generate reverse flow on the ceiling of the test section. Both experiments used a pressure difference to remove air from the diverging section to aid the induction of separation. One tunnel used a compressor to increase the test section pressure and bled air to the outside, while the other used a vacuum pump. Mohammed-Taifour was able to achieve reverse flow velocities of up to 20% of the free stream flow in the separated region; however, neither study published values of the suction flow rate used to create the adverse pressure gradient.

These diverging wind tunnel sections were used as an inspiration for the geometry of the flat plate diffuser. For the suction strength, separation control studies were chosen for a baseline with the idea that if a suction system would prevent separation over a plate, it would induce separation over a wall.

Alrefi and Acharya (1996) used continuous suction over a 30 cm chord NACA 0012 airfoil to delay dynamic stall. The suction system consisted of a 5-part plenum chamber inside the airfoil connected to a 0.5 mm slot located at 2% airfoil chord and a vacuum chamber. By varying the volumetric suction flow rate Q_s , separation could be controlled. The dimensionless suction

flow rate (Eq. 11) required to control separation varied with angle of attack. For example, a \dot{Q} of 0.0017 was needed for 26° , 0.0028 for 29° , and 0.0074 for 35° .

$$\dot{Q} = \frac{Q_s}{u_\infty c^2} \quad (11)$$

Huang *et al* (2004) studied the effects of suction through a slot on a NACA 0012 airfoil through numerical simulation. The study used a slot at 2.5% of the airfoil's chord, varying suction strength, slot location, and suction angle. Results showed that perpendicular suction from 3 to 12% chord length along the airfoil produced optimum separation control. For an angle of attack of 18° , this study found that full separation control was possible with a dimensionless suction rate of 0.01. This \dot{Q} found by Huang *et al* was roughly ten times larger compared to the Alrefi and Acharya experiment, though this increase in required suction may be attributed to the dynamic pitching behavior used in Alrefi and Acharya's experiment.

For the diffuser used in this experiment, dimensionless suction values of the previous studies were chosen as targets. The final flat plate diffuser design was modeled after the airfoil used in Alrefi and Acharya's experiment. The plate has a chord length of 30 cm, a span of 81 cm, and is 0.5 cm thick. A 6 mm slot is located at 8% chord. A plenum chamber 4 cm tall and 3.5 cm wide is attached to the leading edge of the plate, which is divided into 5 sections to equalize suction along the full slot length. The entire plate is attached to a set of brackets located beside the plate, which are attached to the floor of the wind tunnel. The plate is capable of being raised and lowered from the floor of the tunnel in 1.9 cm increments, moved in the streamwise direction in 1.9 cm increments, and set to any angle of attack between 0 and 45° . Fig. 2.19 shows a schematic of the design, while Fig. 2.20 shows the completed plate in the wind tunnel.

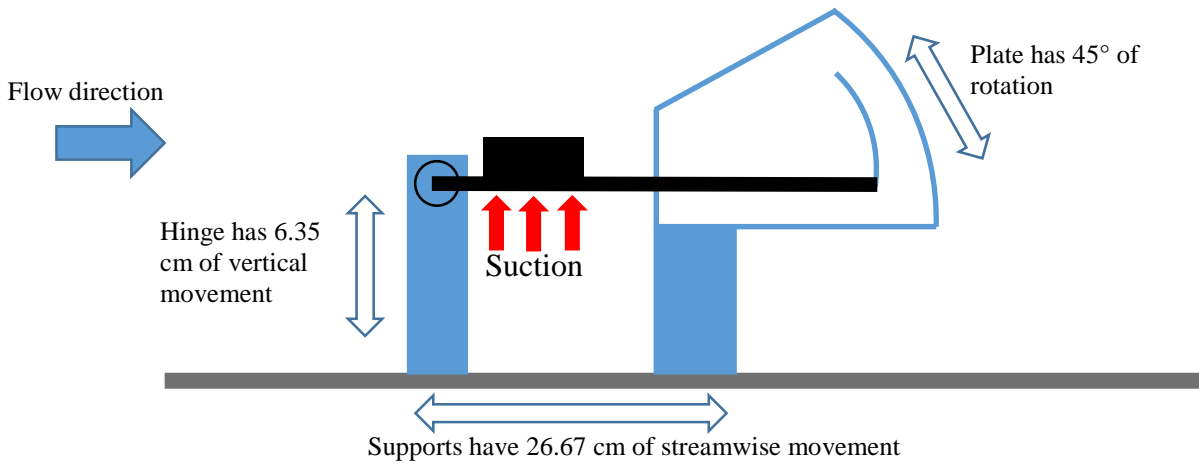


Figure 2.19 Schematic of flat plate with suction



Figure 2.20 Rear view of plate and suction tubes

To provide suction, the plenum chamber was connected to a Vaccon CDF 1000H venturi vacuum generator through 1.905 cm nylon tubing and PVC piping. High pressure compressed air was supplied to the venturi, generating a partial vacuum and drawing air through the tubing

connected to the plate. The CDF 1000H is capable of generating flow rates over 4000 liters per minute (L/min) and vacuum pressures over 10 kPa relative to atmosphere. However, flow rate and vacuum levels are inversely proportional. The maximum vacuum level is only obtainable when zero flow passes through the venturi; likewise, at maximum flow rate the generated vacuum level is heavily reduced. Performance data of the CDF 1000H provided by the manufacturer is shown in Fig. 2.21.

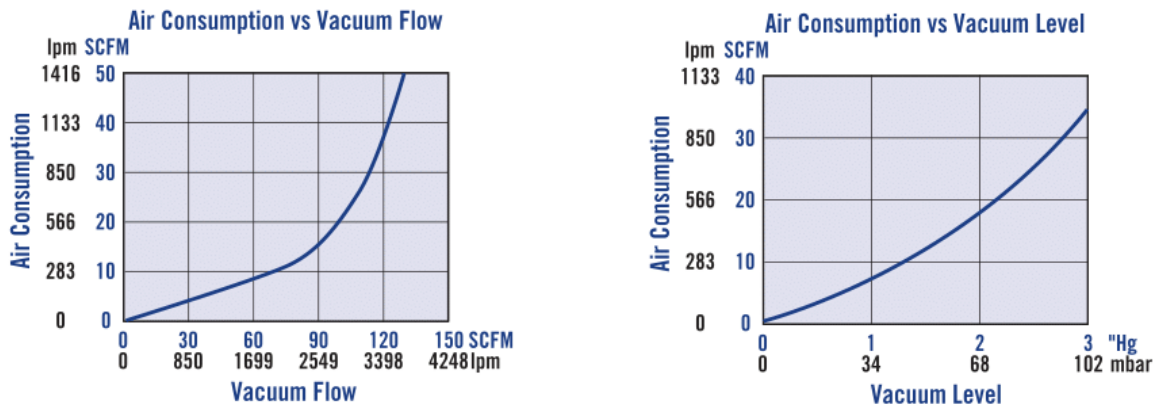


Figure 2.21 CDF 1000H performance data specified by manufacturer

By altering the flow rate of the compressed air supplied to the venturi, the pressure of this supplied air, and the venturi geometry, the vacuum level generated by the venturi could be altered. A Heise model PM pressure scanner (0.1% accuracy) was connected to the venturi to measure vacuum levels. Using the Colebrook (Eq. 12), Darcy-Weisbach (Eq. 13), and minor loss (Eq. 14) equations (White, 2008), major and minor pressure losses through the flat plate and tubing system were estimated.

$$\frac{1}{\sqrt{\lambda}} = -2 \log \left(\frac{k}{3.7D_h} + \frac{2.51}{\sqrt{\lambda} Re} \right) \quad (12)$$

$$\Delta P_{major} = \lambda \frac{L}{2D_h} \rho u^2 \quad (13)$$

$$\Delta P_{minor} = \xi \frac{1}{2} \rho u^2 \quad (14)$$

By knowing the pressure difference from the wind tunnel to the venturi, suction flow rate through the plate could be estimated (Table 2). The final system was capable of generating vacuum pressures relative to atmosphere of up to 15.9 kPa (with zero flow through the system) (Fig. 2.23). Maximum suction flow rate achieved was 2180 L/min; system head loss at this flow rate was 3.86 kPa (Fig. 2.24).



Figure 2.22 CDF 1000H venturi

Table 2. Estimated flow rate through flat plate diffuser

Supply Pressure (kPa)	Flow rate estimate (L/min)	Q_s (m ³ /s)
34	654	0.01
68	832	0.013
103	1100	0.018
137	1318	0.022
172	1566	0.026
206	1704	0.028
241	1833	0.03
275	2002	0.033
310	2131	0.035
330	2180	0.036

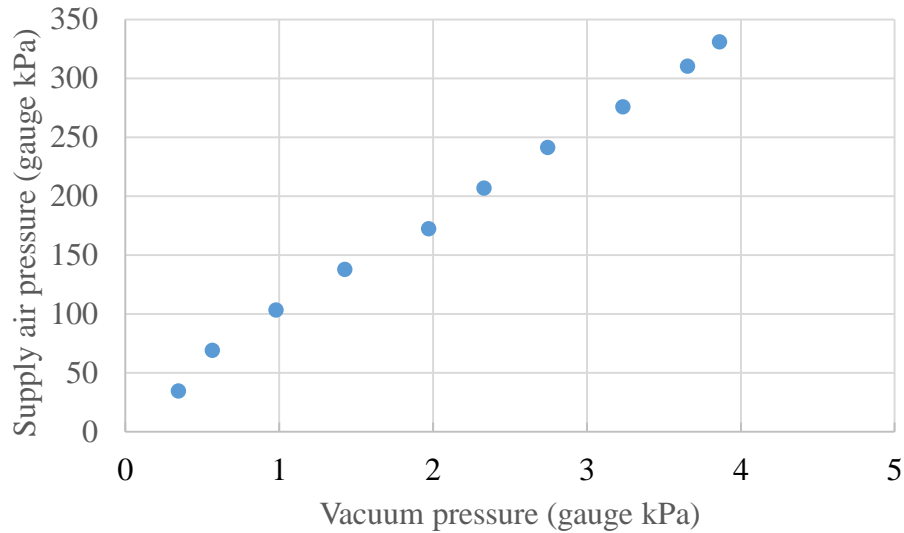


Figure 2.23 Vacuum pressure between wind tunnel and plenum chamber

Using the suction flow rate estimations above, the \dot{Q} of the system was calculated. At 10 m/s, the plate could achieve a maximum \dot{Q} of 0.04, at 20 m/s 0.02, and at 30 m/s 0.013. Following the work of Huang *et al* (2004), this would theoretically be sufficient suction for full separation control at 18° angle of attack.

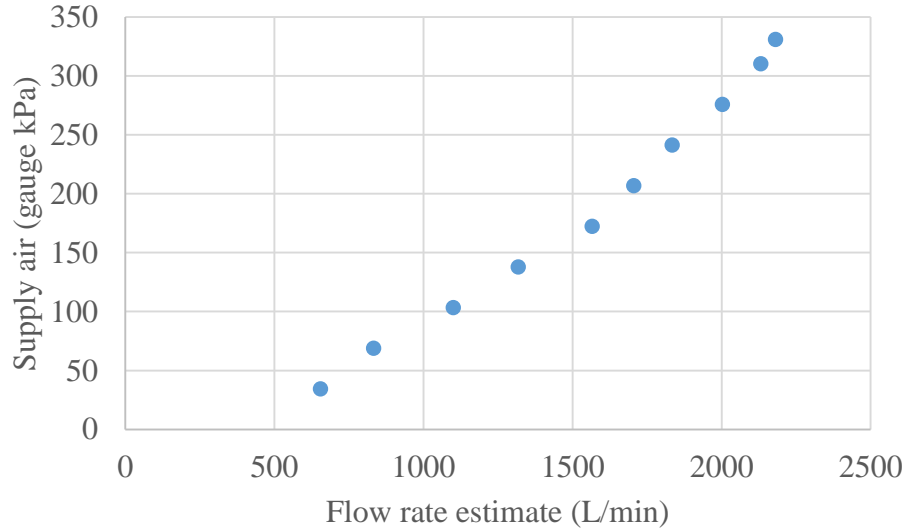


Figure 2.24 Estimated flow rate through flat plate diffuser

2.4 Solid Fence to Induce Separation

Due to the experimental nature of the flat plate diffuser, a secondary method was desired for generation of a separated flow region to compare with the flat plate diffuser. Solid fences were chosen for simplicity. Governing factors for fence-fluid interaction include the fence height H , Re_H (Eq. 15), and boundary layer to fence height ratio $\frac{\delta}{H}$.

$$Re_H = \frac{\rho u H}{\mu} \quad (15)$$

Solid fences are a well-researched cause of separation bubbles, which generate reversed flow downstream and upstream of the fence. Orellano and Wengle (2000) performed DNS of flow over a fence at Re_H of 3,000 and 10,000 and $\frac{\delta}{H}$ of approximately 1. This study estimated the separation region downstream of a fence to be up to $13H$ and the separation region in upstream

of a fence to be up to $2H$. The highest reverse flow velocities occurred between $4H$ and $6H$, up to approximately 30% of the free-stream values for the Re_H 3,000 case.

Van Ratingen *et al* (2013) performed PIV measurements behind 5 and 10 cm solid fences at 10 m/s. The boundary layer was grown over a 15 m test section, making $\frac{\delta}{H}$ large. Streamwise ranges were from 0 to $2H$ upstream and 0 to $18H$ downstream of the fences. The separation bubble behind the fence was estimated to be $10H$ for the 5 cm fence, with reverse flow velocities reaching a maximum of 20% from $2-7H$ downstream. Fig. 2.25 shows the average velocity measurements upstream and downstream of a 5 cm fence (van Ratingen *et al*, 2013).

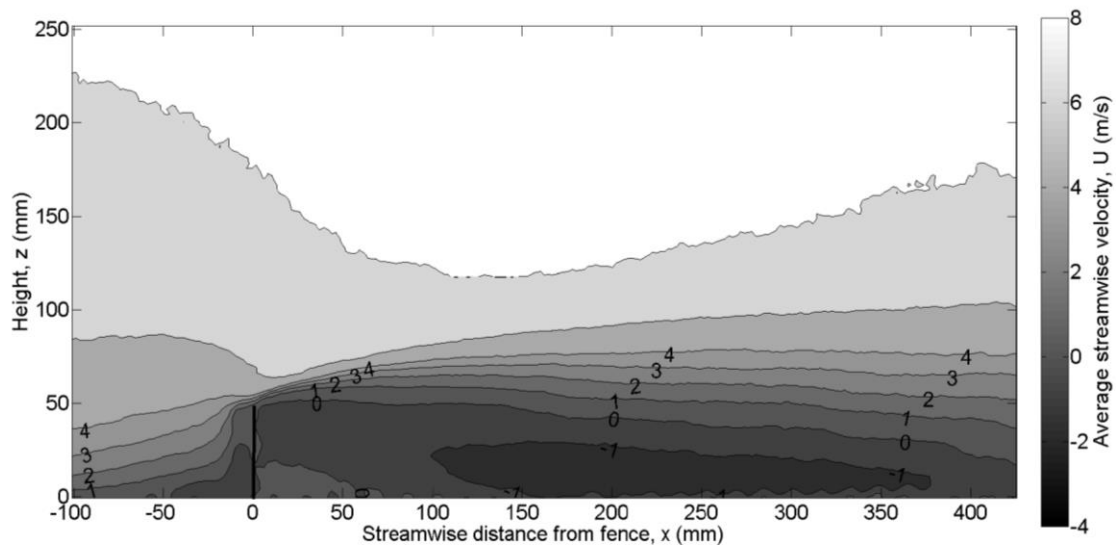


Figure 2.25 Velocity measurements behind a 5 cm fence at 10 m/s (van Ratingen *et al*, 2013)

Two solid fences were chosen to be used in the microflap tests to create a separation region, one 1.9 cm tall and one 3.8 cm tall. These fences were placed at the center of panel 7, 3.91 m from the start of the test section. At test speeds of 10, 20, and 30 m/s, this resulted in Re_H values between 11,720 and 35,160 for the 1.9 cm fence and 23,440 and 70,320 for the 3.8 cm

fence. Because the boundary layer height at this location was a minimum of 4.61 cm, the fences were fully enclosed in the boundary layer for all test speeds. Table 3 shows the estimated Re_H and $\frac{\delta}{H}$ for all test cases.

Table 3. Reynolds number and boundary layer thickness ratios of solid fences in test section

	Fence Height (cm)	10 m/s	20 m/s	30 m/s
Streamwise Re_x	1.9 and 3.8	2.4×10^6	4.81×10^6	7.21×10^6
Re_H	1.9	1.17×10^4	2.34×10^4	3.51×10^4
	3.8	2.34×10^4	4.68×10^4	7.03×10^4
$\frac{\delta}{H}$	1.9	3.02	2.63	2.43
	3.8	1.51	1.31	1.21



Figure 2.26 3.8 cm fence placed in wind tunnel test section

2.5 Test Procedures

The first sets of experiments were performed on the 2D microflaps. The array was placed in the wind tunnel at the center of panel 7, 3.91 m from the start of the test section. The microflap array was oriented in the opposite direction as the scales would be on a shark's body (i.e. oriented with the tip of the microflap facing upstream) (Fig. 2.27). This was done to identify what reverse flow velocities would be necessary to cause the 2D microflaps to bristle. The wind tunnel speed was increased by amounts of 2.5 m/s until 30 m/s.



Figure 2.27 2D microflaps placed in reverse orientation

2D microflaps were also tested in the standard orientation, with the tip of the microflap pointing downstream. 2D microflaps were tested 4H downstream of a 1.9 cm fence to create a region of reverse flow and identify at what speeds the 2D microflaps would bristle. Due to friction and the center of mass being located over the pivot point, the microflaps could be pre-bristled and would remain bristled until acted on by another force (Fig 2.28). The 2D microflaps were pre-bristled and placed in the wind tunnel with no fence to identify if the airflow would cause them to fall back downwards to the resting orientation.



Figure 2.28 Pre-bristled 2D microflaps

Each 2D microflap test case was performed with smooth variants of the microflaps and variants with longitudinal riblets. This was to identify if riblets would influence the speeds that the 2D microflaps would bristle. For all test cases, a digital camera (16 MP, f/2.2, 31 mm focal length) was used to record video (60 Hz) of the tests, which could be reviewed to ensure accurate observations of the tests.

The 3D microflaps were tested in a wider variety of experimental conditions. These included the microflaps placed in the reverse orientation, being pre-bristled with no obstructions in the test section, placed various distances downstream of 1.9 and 3.8 cm fences, placed directly upstream of 1.9 and 3.8 cm fences, placed underneath the flat plate diffuser at various locations along the chord length, and placed upstream of a solid fence combined with the flat plate.

For all 3D microflap tests, several rows of nylon tufts 3 cm long were placed in the wind tunnel to identify flow direction. The tufts were used to visually characterize the locations where reverse flow appeared to be the strongest. These tufts were also placed on the flat plate diffuser to identify flow conditions over the plate.

For the 3D microflaps in the reverse orientation and pre-bristled test cases, the test was performed identically to the 2D microflaps. Test speeds ranged from 5 to 30 m/s. For the solid

fence tests, the array of 3D microflaps was placed with the first row of the array various fence heights downstream of the solid fence. The experimental procedure was repeated for each case, with the wind tunnel speed being increased in each case from 5 to 30 m/s and microflap actuation being recorded by the camera. Fig. 2.29 shows the 3D microflaps 4H downstream of the 3.8 cm fence.



Figure 2.29 3D microflaps 4H downstream of 3.8 cm fence

For tests performed with the 3D microflaps placed under the flat plate diffuser, several different test configurations were used. Tests were conducted by first setting a position and angle for the plate, then turning on the wind tunnel. At various speeds from 5-30 m/s, the suction level was increased. Microflap activity was recorded using the camera. Fig. 2.30 shows the 3D microflaps underneath the flat plate.



Figure 2.30 3D microflaps underneath flat plate diffuser

The second group of solid fence tests involved the 3D microflaps being placed directly upstream of the fence. The front of the microflap array was $2.66H$ upstream of the 1.9 cm fence and $2H$ upstream of the 3.8 cm fence. The flat plate diffuser was also used to encourage flow separation upstream of the fences. Fig 2.31 shows a setup of the microflaps in front of the solid fences.

To obtain velocity measurements of the separated region downstream of the solid fence, a TSI 1750 constant temperature anemometer and 1210-20 hot film probe were used. The probe was placed in the center of panel 7 (3.91 m from the start of the test section) in a streamwise slot 18 cm long. A Velmex XN10-0120-E25-21 linear slide was used to move the probe along the length of the slot (Fig. 2.32). The wire was oriented in the spanwise direction, resulting in a measurement of velocity magnitude in the x-y plane of the flow.



Figure 2.31 3D microflaps upstream of 3.8 cm fence

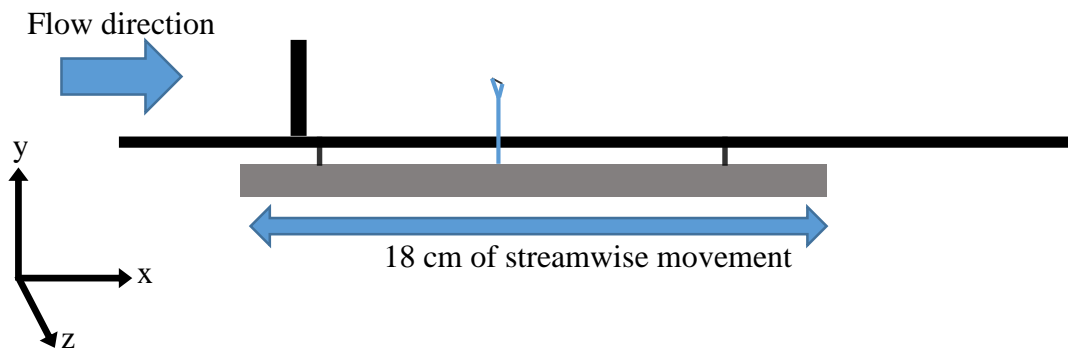


Figure 2.32 Schematic of hot film probe behind solid fence

The 3.8 cm fence was placed 0, 13, and 28 cm upstream of the slot to generate a separated flow region. The hot film probe was placed $1H$, $0.5H$, and $0.15H$ vertically from the floor. The probe was moved in 1 cm increments in the streamwise direction downstream of the fence at 10, 20, and 30 m/s. This resulted in streamwise coverage from $1H$ to $12H$ downstream of the fence. At each streamwise position, 15,000 voltage readings were acquired at 3,000 Hz.

The hot film probe was calibrated for each day of testing; calibration was performed by using a pitot-static probe in the free stream at the same downstream distance as the hot film probe and measuring voltage and velocity from 0 to 36 m/s in 3 m/s increments. After calibration was completed, a fifth order polynomial (Eq. 16) was used to calculate velocity from the voltages measured during the tests.

$$u = A_0 + A_1V + A_2V^2 + A_3V^3 + A_4V^4 + A_5V^5 \quad (16)$$

During testing, it was noted that leaving the hot film probe powered on for continued periods of time resulted in drops in voltage readings. After an initial period of approximately 2 minutes while the sensor warmed up, the voltage readings decayed at a constant rate of 1% every 5 minutes the probe remained powered on. The cause of this decay is unknown; to attempt to mitigate this decay, for each test performed involving the hot film probe the probe was switched on for 10 minutes before taking any measurements.

As mentioned in the previous pages, the 2D and 3D microflaps were placed in several different configurations and flow conditions. Some tests differed from others in their purpose and type of data gathered. Table 4 lists all tests performed, a description of the tests, the conditions during the tests, and the purpose of performing the tests.

Table 4. Total test matrix

Test type	Test setup configurations	Test conditions	Test objectives
2D microflap bristling test	2D microflaps placed in reverse orientation	Speed raised in 2.5 m/s increments from 0 to 30 m/s	Identify boundary layer speeds needed to bristle 2D microflaps
3D microflap bristling test	3D microflaps placed in reverse orientation	Speed raised in 2.5 m/s increments from 0 to 30 m/s	Identify boundary layer speeds needed to bristle 3D microflaps
3D microflap reverse flow fence test (downstream of fence)	3D microflaps placed 1H, 2.66H, 3H, 4H, 8H, and 12H downstream of 1.9 and 3.8 cm fences	Speed raised in 5 m/s increments from 0 to 30 m/s	Identify distances behind fence with reverse flow sufficient for bristling
3D microflap reverse flow fence test (upstream of fence)	3D microflaps placed directly upstream of 1.9 and 3.8 cm fence (front row of microflap array 7.62 cm upstream of fence, or 2.66H and 2H)	Speed raised in 5 m/s increments from 0 to 30 m/s	Identify distances in front of fence with reverse flow sufficient for bristling
Flat plate diffuser test	3D microflaps placed under flat plate diffuser from 0-130% chord length. Plate set at 0, 10, 20, and 25° 10 and 13.3 cm from the wind tunnel floor.	Speed raised in 5 m/s increments from 0 to 30 m/s, vacuum flow altered from 0 to 2000 L/min	Test ability of diffuser to create reverse flow region in wind tunnel and if sufficient reverse flow for bristling
Combination test	3D microflaps placed directly in front of 3.8 cm fence, 130% of chord from flat plate diffuser set 13°.	Speed raised in 5 m/s increments from 0 to 30 m/s, suction flow altered from 0 to 2000 L/min	Test ability of microflaps to bristle in combination with both reverse flow generation methods
Hot film anemometry of flow behind solid fences	Hot film probe swept in streamwise direction from 1H to 24H behind 3.8 cm fence. Sweeps taken at 3.8, 1.9, and 0.5 cm above tunnel floor (1H, 0.5H, and 0.15H)	Speeds raised in 5 m/s increments from 5 to 30 m/s, probe moved in 1 cm streamwise increments. 15,000 voltage measurements taken at each point at 3,000 Hz.	Measure velocity values behind fence to compare with previous fence velocity studies.

CHAPTER 3: RESULTS AND DISCUSSION

After the 2D and 3D microflaps were constructed, they were placed in the University of Alabama low-speed wind tunnel and tested in a variety of flow conditions. The primary goal was to identify and understand the conditions within the lower 5% of the boundary layer that would cause the microflaps to actuate. This section explains the flow conditions in which microflaps could be actuated by the flow. Microflaps were observed to actuate in several conditions, but 3D microflaps actuated the most and fluctuated when placed 12H downstream of a solid fence as well as 2H upstream of a solid fence combined with flat plate suction.

3.1 2D Microflap Results

The 2D microflaps were designed and tested before the 3D variants. This was planned as a proof-of-concept test to identify if flow in the lower 5% of the boundary layer could actuate the microflaps. Feedback and results from the 2D microflap tests were implemented when designing the 3D microflaps. As a result, the 2D microflaps were not tested in as many flow conditions as the 3D microflaps.

The 2D array consists of 12 rows of 2D microflaps with a 4.88 mm chord length and 10.8 cm span length. The array was placed 3.91 m downstream of the start of the test section. The boundary layer in this location was measured to be approximately 7 cm at 15 m/s. Most tests performed on the 2D microflaps involved arranging the 2D microflaps in the reverse orientation

(with the tip of the 2D microflaps pointed upstream). All tests with the 2D microflaps were performed once using smooth 2D microflaps and once using 2D microflaps with longitudinal riblets placed every 1.05 mm along the span.

Several problems were identified during the testing of the 2D microflaps. Due to manufacturing differences, some microflaps were in closer contact with the brass rods than others, causing additional friction. After being manufactured, the microflaps warped due to their long aspect ratio resulting in expansion and contraction of different layers of the 3D printing material. Another issue was that the airflow caused the 2D microflaps and the brass axles to permanently bend. In subsequent tests the axle constantly rubbed against the hinge of the 2D microflaps, limiting rotation.

For the reverse orientation test of the smooth 2D microflaps, flap actuation was first observed at 8 m/s (fifth row, 50°). At approximately 25 m/s, the row farthest upstream bristled fully and the fifth row simultaneously dropped down. This is likely caused by the protrusion of the first microflap into the flow, creating an area of slowed flow behind it. Fig. 3.1 shows a time lapse of this effect. As speed was lowered, the first upstream row began to fall, coming to rest at approximately 20°.

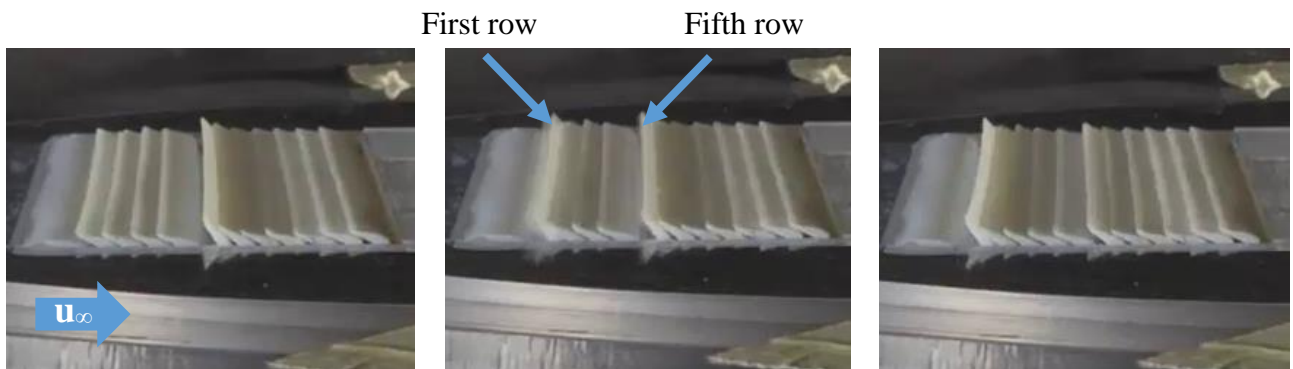


Figure 3.1 0.5 second time-lapse of 2D microflap bristling and downstream microflap dropping

The riblet 2D microflaps behaved similarly to the smooth ones. At approximately 9 m/s, the fifth row of the array bristled to 50° , and at 15 m/s the first row of the array bristled fully and the fifth row dropped down. Due to the center of gravity of the microflaps, they remained bristled while at their maximum rotation of 60° and did not fall downwards unless acted on.

To investigate the effect of the front row rising and the rows downstream of it falling, the 2D microflaps were also tested with the tip of the microflaps pointed downstream and all rows manually pre-bristled. At approximately 19 m/s, the microflap array developed an alternating pattern: roughly every other row had begun to fall downwards and rested against the row downstream of it (Fig. 3.2). Additional rows began to fall as speed increased (Fig. 3.3).



Figure 3.2 Alternating pattern of pre-bristled 2D microflaps being pushed down by flow



Figure 3.3 Pre-bristled 2D microflaps pushed down at 27 m/s

2D microflaps were also placed $6H$ downstream of a 1.9 cm fence ($\frac{\delta}{H}$ between 2.43 and 3.02). Tunnel speed was increased up to 40 m/s; however, actuation was not observed. In reverse flow tests, the 2D microflaps began to bristle between free-stream speeds of 8 and 15 m/s. These speeds are consistent with reverse flow velocities expected behind the solid fence (van Ratingen *et al*, 2013). Unlike the reverse orientation tests, however, reversed flow formed behind a fence is three-dimensional, meaning across the span of a single 2D microflap flow would not be consistently reversed. This could explain why the 2D microflaps were unable to be actuated in the reverse flow scenario.

As a proof-of-concept design, the 2D microflaps were able to prove that airflow in the lower 5% of the boundary layer could actuate an object. However, consistency between tests was an issue. In repeat tests, different rows would bristle in place of previous ones. For example, in the reverse orientation tests the second row would sometimes bristle instead of the first and the sixth row would bristle instead of the fifth. These consistency issues are hypothesized to be due to design flaws with the 2D microflap array. Manufacturing differences between microflaps caused some to come into closer contact with the brass axles than others, causing additional friction. Warping due to 3D print material expansion and contraction as well as deformation due to the airflow also contributed to inconsistency between rows and additional friction.

For the above reasons, the 3D microflaps were designed to use a different method of attachment and 2D microflaps were no longer used in other tests. Instead of solid rods, A228 steel music wire (diameter of 0.05 cm) was used as the central axle for the 3D microflaps. This wire was tensioned with the goal of increased stiffness compared to the relatively malleable brass rods. The wire was also of a smaller diameter than the rods, lowering contact area between the

axle and 3D microflaps. The lowered surface area of each individual 3D microflap compared to the 2D microflaps meant that each would be in contact with less of the axle, meaning that even if the wire became deformed due to high load each individual 3D microflap would be able to rotate. This lower surface area would also allow the 3D microflaps to more easily be actuated by intermittent bursts of reverse flow occurring in different spanwise positions.

3.2 3D Microflap Bristling Results

After being manufactured and installed, friction was still present between the 3D microflaps and the tensioned wires. Graphite powder was also applied to the 3D microflaps to attempt to reduce this. Unlike the brass rods, the tensioned wire system did not permanently deform when load was applied to it, so throughout all tests the 3D microflaps were able to rotate around the axle. Some space was intentionally left in each row so microflaps would not be squeezed together and increase side contact friction. However, as the 3D microflaps could slide along the wires in the spanwise direction, different groups of microflaps along a row could become bunched together while others formed gaps. This meant that certain microflaps on a row would rotate while others on the row would not rotate due to friction. Before each test, 3D microflaps were spaced out evenly to keep start conditions uniform.

The first tests performed on the 3D microflaps were a direct bristling comparison to the 2D microflaps. The 3D microflaps were placed 3.91 m downstream from the start of the test section in the reverse orientation (with the tip of the microflaps pointing upstream). The first 3D microflap activity was seen at a free-stream speed of 10 m/s, where the first two upstream rows in the 3D microflap array became fully bristled. Although the microflaps were designed to only bristle to a maximum of 60° , the microflaps in the front row rotated beyond this point to a

maximum of 90° , where the foot stopped against the wall in front of it (Fig. 3.4 A). Due to manufacturing tolerances, the wire to floor gap for each row of microflaps varied; larger gaps on some rows prevented the foot of the microflap from correctly engaging with the floor. The wires were also not able to be tensioned to the desired levels, meaning each row could temporarily deform when force was applied on them, creating a similar effect.

At 20 m/s, additional microflaps began to bristle to approximately 30° (Fig. 3.4 B). At 25 m/s, several microflaps in the back half of the array bristled, with about a quarter of the total microflaps on the array bristled in some form (Fig. 3.4 C). As speed was increased to 30 m/s, additional microflaps in clumps began to bristle in the front and back halves of the array (Fig. 3.4 D).

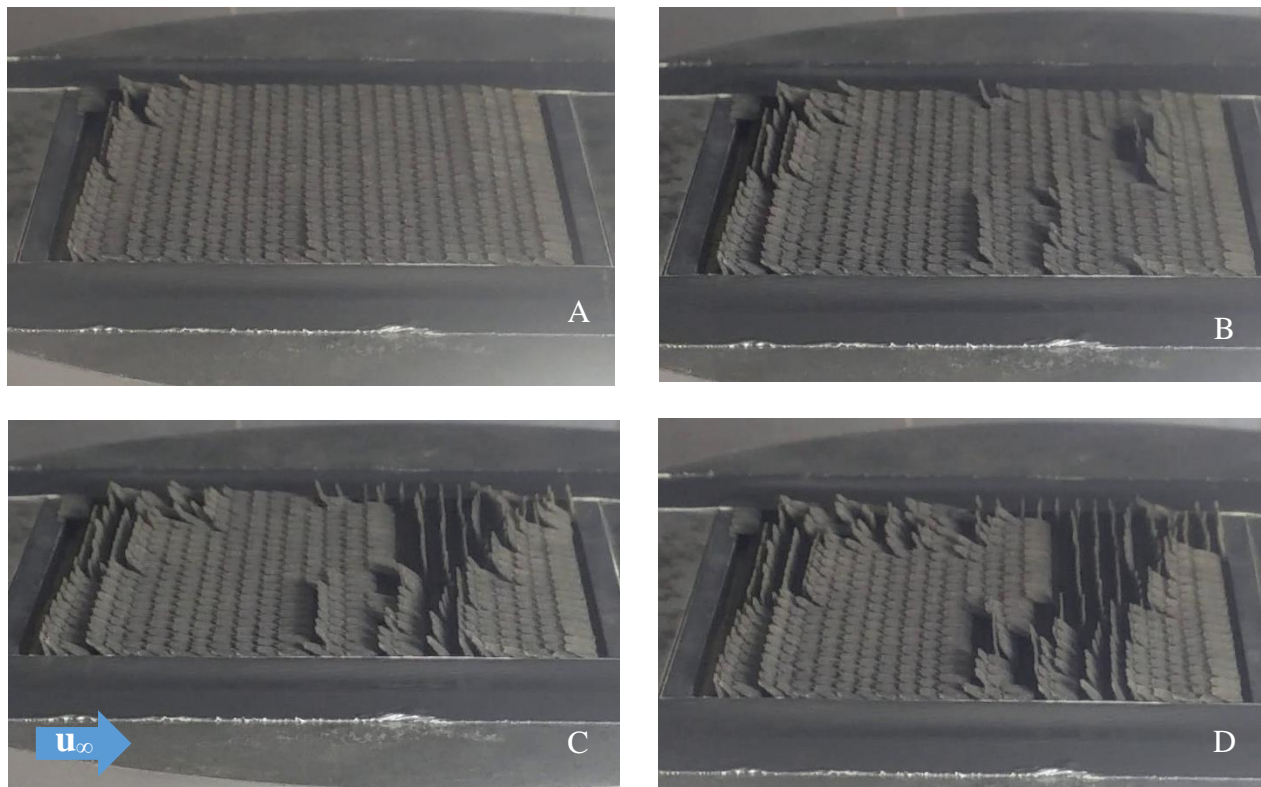


Figure 3.4 3D microflaps bristled by reverse flow at various speeds. 10 m/s (A), 20 m/s (B), 25 m/s (C), and 30 m/s (D)

Microflaps at different locations in the array became bristled to different angles. At 30 m/s, some microflaps bristled to the maximum designed angle of 60°. Others rotated to 90°, while others bristled between 10 and 50° (Fig. 3.4 D). As tunnel speed was lowered to 0 m/s, no changes were observed to the 3D microflaps. Like the 2D microflaps, the center of gravity of the 3D microflaps meant microflaps would not return to rest unless acted upon.

Although the 3D microflaps are capable of actuating individually, microflaps tended to bristle as a row. This is believed to be due to friction between the 3D microflaps; one 3D microflap in the process of bristling would rub against the microflap next to it. However, not every microflap in the row reached the same bristling angle.

To determine if the 3D microflaps could return to their resting position after being bristled, the 3D microflaps were placed with the tip of the microflaps pointing downstream and manually pre-bristled to an angle of 90°. At a free-stream speed of 18 m/s, a few microflaps were pushed down by about 10°. As speed increased, greater numbers of microflaps began to be pushed down. Above 30 m/s, a few microflaps returned to the flat resting position, but most of the microflaps did not move from their maximum bristling angle at all (Fig. 3.5). This trend would be seen in later 3D microflap tests; once a 3D microflap became bristled, it would not usually return to the resting position.



Figure 3.5 Pre-bristled 3D microflaps at 30 m/s; most microflaps are not pushed down

In summary: the 3D microflaps began to be actuated at similar speeds to the 2D microflaps (about 10 m/s), and once a row of the array had been bristled it generally prevented rows directly downstream from it from being bristled as well. One major difference in the microflaps was that the 3D microflaps were generally not able to return to the resting position after being bristled, even when reverse flow at speeds upwards of 30 m/s was acting on them. This was due to the 3D microflap design. Although the tensioned wire was designed to prevent movement of the rows, the wires stretched from their normal positions temporarily when under load. This allowed individual microflaps to over-rotate to 90° . When the load on the microflaps was released, the wire returned to its normal position, trapping the foot on the basin and preventing the microflap from returning to the resting position. If the 3D microflaps did not reach their maximum designed bristling angle, then they were able to fall back downward to the resting position, but if over-rotated remained bristled.

3.3 Fence Downstream Velocity Profiles

For comparison to previous published studies, streamwise velocity profiles were acquired for the 3.8 cm fence ($\frac{\delta}{H}$ between 1.21 and 3.81). Data was obtained at 10, 20, and 30 m/s from 4 to 45 cm downstream of the fence (corresponding to 1H and 12H) with probe heights 3.8, 1.9, and 0.5 cm from the wind tunnel floor (corresponding to 1H, 0.5H, and 0.15H). All measurements were of absolute value of a velocity vector in the x-y plane of the flow. Identifying the direction of this vector with a single-wire fence was not possible, but is assessed based on the literature of flow behind a fence.

The velocity profiles for the 1H probe height were similar in the streamwise direction. Velocity values varied only slightly, between 20 and 30% of the free-stream velocity (Fig. 3.6). Relative velocity measurements to the free-stream were the smallest out of all three probe heights tested, reaching a maximum of 30%. All three test speeds follow a consistent pattern throughout the streamwise positions. Out of all speeds, 30 m/s showed the lowest velocity, never reaching above 25% of the free-stream velocity. These values are consistent with previous studies on fence profiles at 1H from the floor of the test section (van Ratingen *et al*, 2013). Based on van Ratingen's study (Fig. 3.7), flow at 1H is slightly above the stagnation line. Flow at this height is thus most likely not reversed.

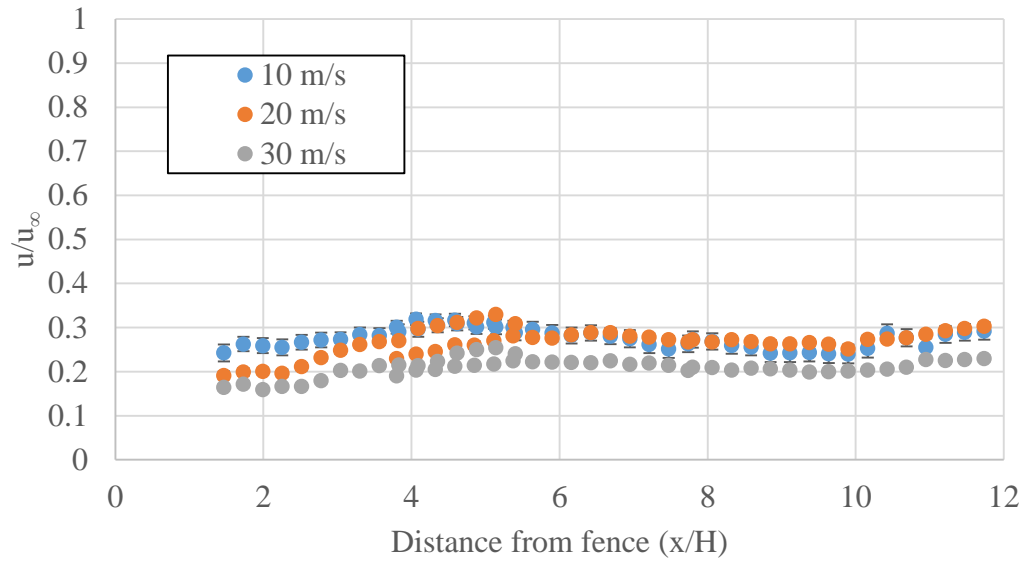


Figure 3.6 Nondimensionalized velocity profiles at 1H vertical distance with standard deviation error bars

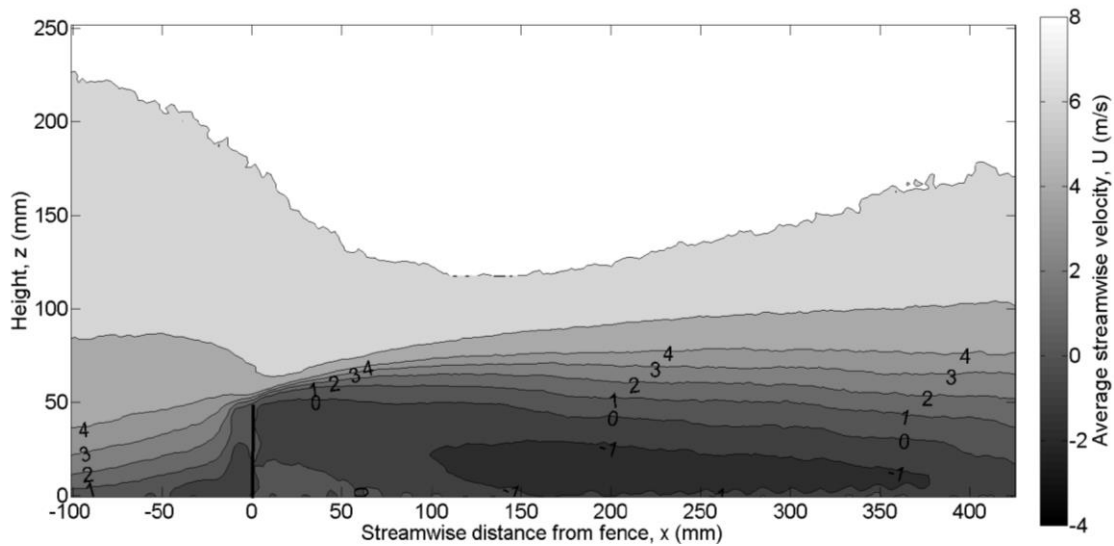


Figure 3.7 Velocity measurements behind a 5 cm fence at 10 m/s (van Ratingen *et al*, 2013)

At a vertical distance of $0.5H$, the velocity profile shapes varied much more in the streamwise direction than in the 1H test (Fig. 3.8). All three test speeds demonstrate a consistent pattern in the streamwise direction, with the only differences in relative flow velocities between

2H and 4H. Maximum values of 40% free-stream velocity occur between 5H and 6H and minimum values of 20% occur at 10H. Relative velocity measurements are an increase from the 1H test. Based on previous studies, this height is below the stagnation line of the fence, so flow is most likely reversed.

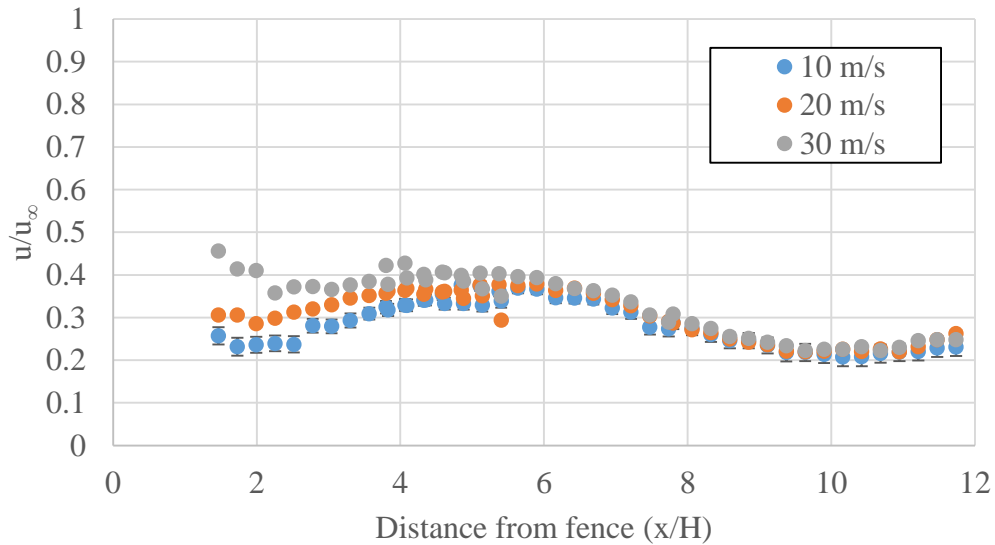


Figure 3.8 Nondimensionalized velocity profiles at 0.5H vertical distance with standard deviation error bars

Velocity profile measurements at 0.15H show the most fluctuation (standard deviation) of the three probe heights tested (Fig. 3.9), especially far downstream of the fence (greater than 10H downstream) near the suspected reattachment zone. All three test speeds follow a consistent shape, with the 2-4H region showing the most difference in relative velocity for all three test speeds. Values range from a maximum 70% free-stream velocity at 2H and 4H and a minimum of 15-20% free-stream velocity at 10-12H. This maximum of 70% was the largest relative velocity measurement of all three test heights; however, 15% is the lowest of all relative velocity measurements.

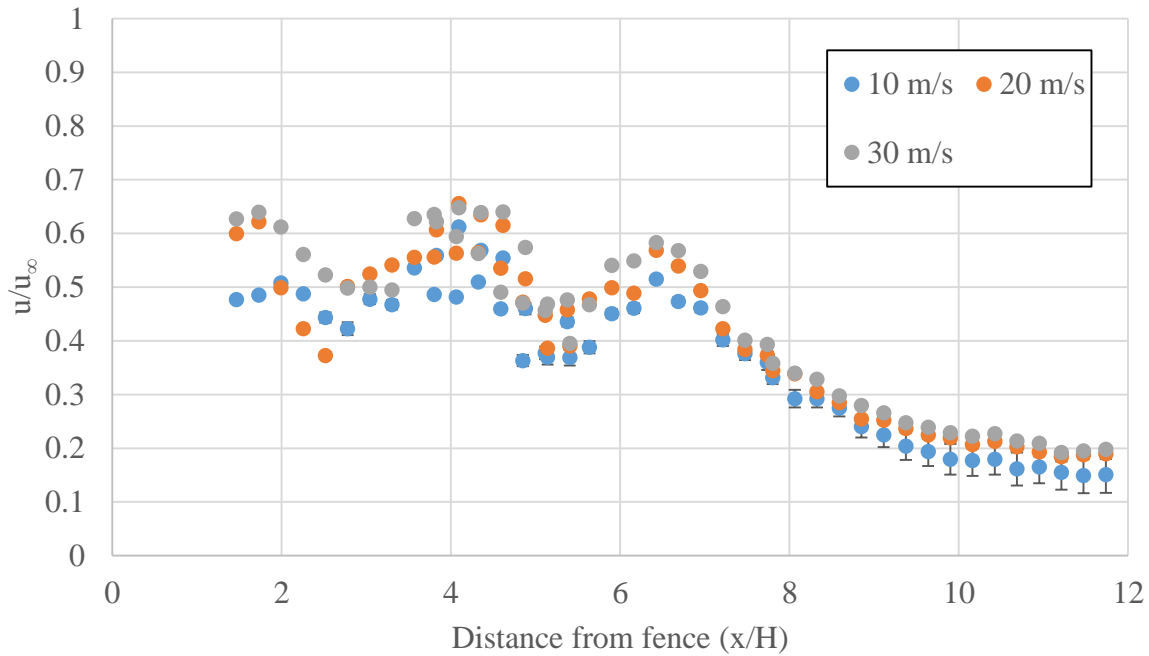


Figure 3.9 Nondimensionalized velocity profiles at 0.15H vertical distance with standard deviation error bars

In previous studies, the region just downstream of the fence (0-2H) transitions between forwards and reversed flow (van Ratingen *et al*, 2013) due to a secondary separation zone. At downstream values greater than 2H, flow is consistently reversed in the primary separation zone. This suggests the flow direction of the velocity measurements at 0.15H vertical distance is reversed. The locations of maximum reversed flow velocities also correspond with previous studies: between 4H and 7H downstream (Orellano and Wengle, 2000). The reattachment zone of the separation bubble is estimated to be 10-12H downstream. The drop in relative velocity measurements downstream of 6H corresponds to this, reaching a minimum of 15%. Due to the correlation between previous studies combined with the increased in variance of each point, flow between 10H and 12H indicates the near proximity to the reattachment zone.

3.4 3D Microflap Fence Results

3D microflaps were placed downstream from 1.9 cm and 3.8 cm solid fences. Each fence was tested with the front row of the array placed 1H, 2.66H, 4H, 8H, and 12H downstream of the fence from 5 to 30 m/s in 5 m/s increments. The microflaps were also tested with the back row of the array placed directly upstream of the fences, making the front row 2.66H upstream of the 1.9 cm fence and 2H upstream of the 3.8 cm fence.

3.3.1 Results 1H Downstream of Fence

For the 1.9 cm fence, initial bristling of the row farthest downstream (4H) was first seen at 15 m/s. At 25 m/s, some microflaps 1H downstream began small fluctuations from flat to approximately 10° at 4 Hz. Microflap frequency was measured by advancing videos by a single frame at a time and counting the number of frames that fluctuation took place. At 30 m/s these microflaps fully bristled to 60° .

The 3.8 cm fence test did not involve any microflap activity until 20 m/s. At this speed, microflaps 1H downstream began fluctuating from 0 to 30° at 4 Hz and microflaps 2-3H downstream bristled fully. By 25 m/s, additional microflaps had bristled (Fig. 3.10). Microflaps 1H downstream ceased fluctuation and bristled fully to 60° , while microflaps 2H downstream began to fluctuate from 0 to 60° .

The location of fluctuating microflaps corresponds with expectations of flow downstream of a fence. Microflaps showed fluctuations between 1H and 2H downstream of the fence, where flow transitions from forward to reverse. At locations farther downstream, no fluctuation was observed, corresponding with constant reversed flow.



Figure 3.10 3D microflaps 1H downstream of a 3.8 cm fence at 25 m/s

The 3D microflaps downstream of the fence first bristled at similar free-stream speeds as the reverse orientation tests (15-20 m/s). On both the 1.9 and 3.8 cm fences, microflaps usually bristled together as an entire row. If a row of microflaps only partially bristled, at the next highest speed the entire row usually became bristled. Similar to the 2D microflaps, when a row of 3D microflaps bristled it prevented rows directly downstream from bristling as well.

3.3.2 Results 2.66 Downstream of Fence

For the 1.9 cm fence, microflaps first bristled at 10 m/s. Between 10 and 15 m/s, the microflaps farthest downstream of the fence (6.66H) bristled fully. Additional microflaps bristled as speed increased; by 25 m/s about half of the array had fully bristled (Fig. 3.11). However, none of the bristled microflaps fluctuated. This corresponds to the velocity profile measurements and previous studies, which showed constant reversed flow in this region.

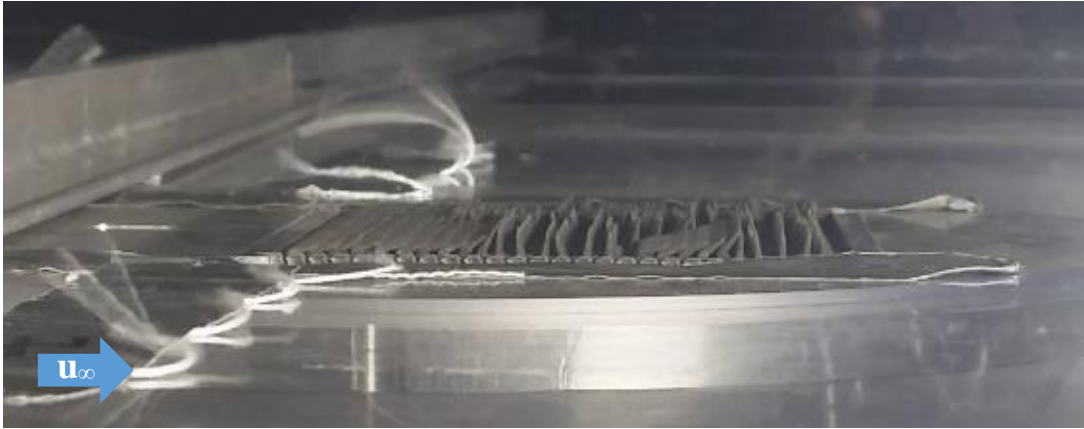


Figure 3.11 3D microflaps 2.66H downstream of a 1.9 cm fence at 25 m/s. Half of the microflaps are fully bristled

The 3.8 cm fence behaved similarly to the 1.9 cm fence. First actuation was observed at 15 m/s on rows farthest downstream of the fence (4.66H). By 30 m/s, approximately three-quarters of the microflaps had fully bristled (Fig. 3.12 B). No fluctuation of any microflaps was observed.

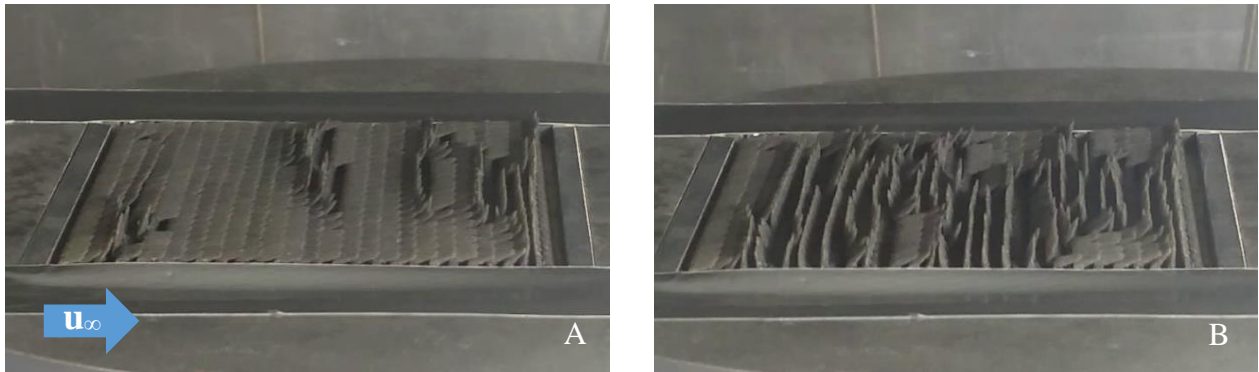


Figure 3.12 3D microflaps 2.66H downstream of a 3.8 cm fence. Test velocity is 20 m/s (A) and 30 m/s (B)

3.3.3 Results 4H Downstream of Fence

For the 1.9 cm fence, microflaps first bristled at 10 m/s. At 15 m/s roughly one-quarter of the microflaps were fully bristled, at 25 m/s roughly one-half, and by 30 m/s roughly 90% of the microflaps had fully bristled.

The 3.8 cm fence behaved similarly, with first bristling of the rows 6H downstream at 10 m/s. At 15 m/s additional rows began to bristle (Fig. 3.13 A). Bristling then began to spread out from the middle rows at 20 m/s (Fig. 3.13 B). By 25 m/s approximately half of the microflaps had bristled, and at 30 m/s approximately 90% were bristled (Fig. 3.13 C).

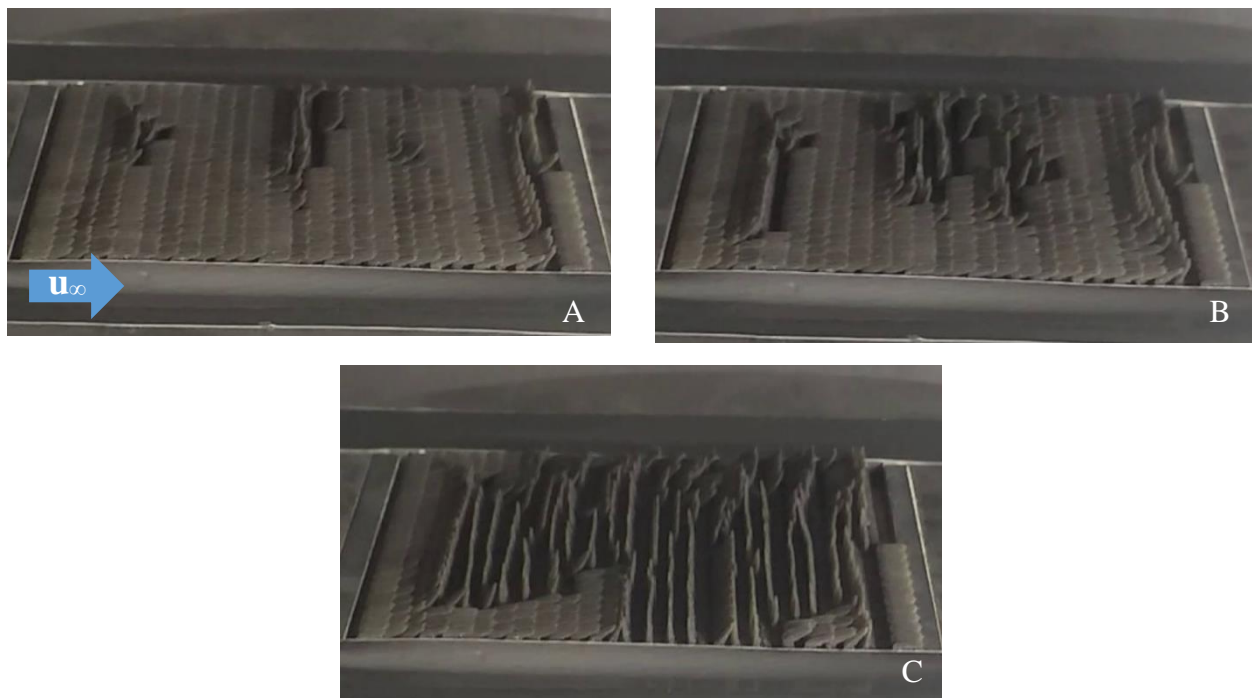


Figure 3.13 3D microflaps 4H downstream of a 3.8 cm fence. 15 m/s (A), 20 m/s (B), 30 m/s (C)

In both the 1.9 and 3.8 cm fence tests, no fluctuation of any 3D microflaps was observed. This region (4H to 7H downstream) had the largest reverse flow velocities measured (at 0.15H from the wind tunnel floor), with a maximum of 70% free-stream velocity. This also corresponds

with previous studies demonstrating the region from 3H to 8H downstream having constantly reversed flow.

The amount of microflaps that bristled in the 4H downstream test was greater than the previous test configurations. At lower speeds, bristling was concentrated only in the back and middle rows. Bristled microflaps blocked rows directly behind them from being bristled, due to each microflap creating a smaller region of separation behind it. However, at high speeds, the flow was strong enough to overcome this and bristle a majority of the microflaps.

3.3.4 Results 8H Downstream of Fence

The 1.9 cm fence first had microflaps bristle at 15 m/s, where some microflaps 9-10H downstream bristled to approximately 30° . At 20 m/s the remaining microflaps 9-10H downstream fully bristled; approximately a quarter of the array was fully bristled at this speed.

Some microflaps 10-12H downstream began to fluctuate at 20 m/s. Various microflaps fluctuated in pulses from 60° to 30° , with about 20% of the pulses instead fluctuating from 60° to 0° . Fluctuation was not constant; microflaps remained fully bristled about 90% of the time and spent the other 10% of the time fluctuating. Fluctuation frequency was a consistent 6 Hz, but for each pulse microflaps could fluctuate multiple times or only once before returning to their fully bristled angle.

Speed was increased to 25 m/s, resulting in approximately three-quarters of the microflaps becoming fully bristled. Microflap fluctuation continued on the previously specified rows, but with a higher frequency of approximately 11 Hz. Additional microflaps 8-9H downstream began to fluctuate as well, but only from 60° to 50° . Only microflaps 9-10H downstream fluctuated fully from 60° to 0° .

The 3.8 cm fence first had microflaps bristle at 10 m/s (Fig. 3.14 A). At 15 m/s, approximately one-fifth of microflaps were fully bristled (Fig. 3.14 B). At 20 m/s another large change occurred, with approximately 70% of all microflaps being bristled at this speed (Fig. 3.14 C).

The microflaps also began fluctuating at 20 m/s. At this speed about 10% of the bristled microflaps underwent constant, small fluctuations of 10° . The rest of the microflaps remained fully bristled and rotated from 90° to 40° in bursts of fluctuation. This bursting process lasted about half a second and occurred about every 2-5 seconds, with each burst involving 30% of the bristled microflaps. The distribution of microflaps involved in each burst was random, but all microflaps were involved in fluctuations throughout the test. Fluctuation frequency was 6 Hz.

At higher test speeds, fluctuation intensified. At 25 m/s, each burst involved 50% of the bristled microflaps and frequency increased from 6 to 11 Hz. Bursts of fluctuation occurred more often, about once per second. By 30 m/s 90% of the array was fully bristled (Fig. 3.14 D). At this speed, every microflap underwent constant 10 degree fluctuations as well as fluctuation bursts.

8H downstream of the fence was the first distance to create widespread bristling and fluctuation across the entire microflap array. At lengths closer to the fences, flow at the wall was steadily reversed. The velocity profile measurements showed a decrease in relative velocity from 8-10H downstream, reaching a minimum of 20%. With the front row of the array 8H downstream, flow over the rows was nearing the reattachment zone, resulting in changes in flow direction.

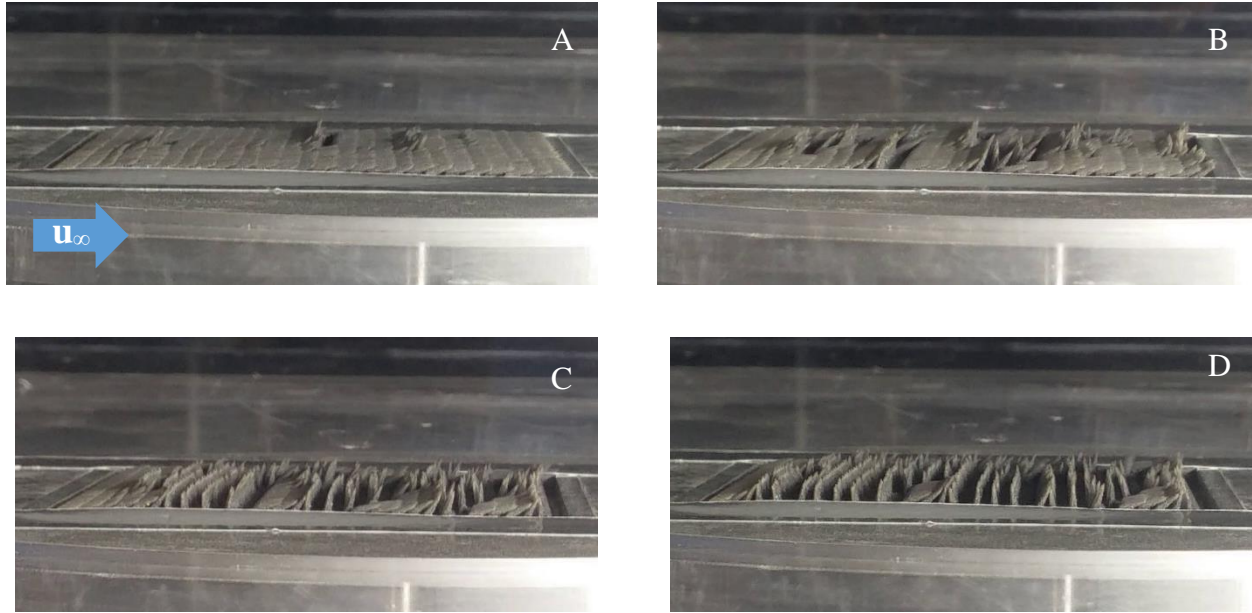


Figure 3.14 3D microflaps 8H downstream of a 3.8 cm fence. 10 m/s (A), 15 m/s (B), 20 m/s (C), 30 m/s (D), top left to bottom right

3.3.5 Results 12H Downstream of Fence

At 12H, the microflaps downstream of the 1.9 cm fence first began activity at 15 m/s, where microflaps 12-13H downstream began fluctuating from 0 to 10° at 4 Hz. Unlike other fence distances, the microflaps began fluctuating before fully bristling. At 18 m/s, the amplitude of the fluctuations increased, with microflaps now rotating from 0 to 40°. At 20 m/s, the fluctuation continued in the previously mentioned microflaps and began spreading to other microflaps around these regions. Fig. 3.15 shows various photographs taken at 20m/s, demonstrating the unsteady bristling of several of the microflaps. At 25 m/s, about a quarter of the microflaps of the array became fully bristled; these microflaps continued to fluctuate from 0 to 90°.

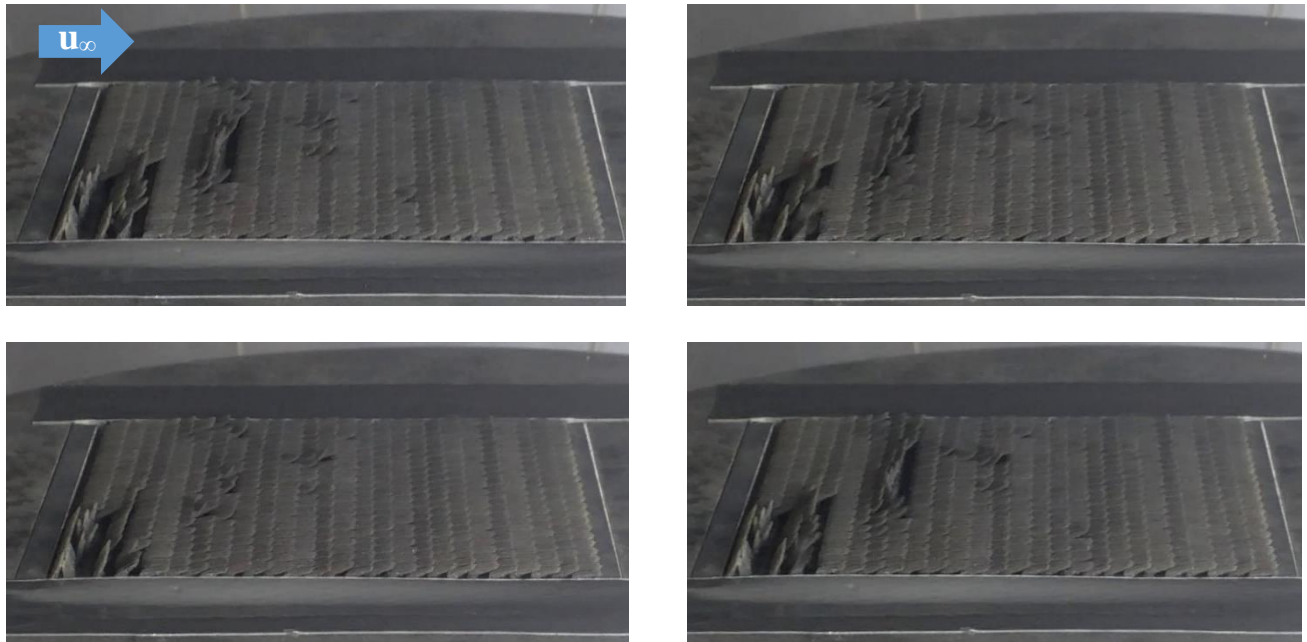


Figure 3.15 Multiple images of fluctuating 3D microflaps 12H downstream of a 1.9 cm fence at 20 m/s

At 30 m/s, microflap fluctuation increased in intensity. About 75% of the microflaps 12-13H downstream fluctuated at 12 Hz. Another 20% of the microflaps in this region of the array remained flat, while the rest stayed fully bristled but did not fluctuate. Microflaps 13-14H downstream also began fluctuating in bursts from 0 to 10°, similar to what had first occurred at 15 and 20 m/s (Fig. 3.16).

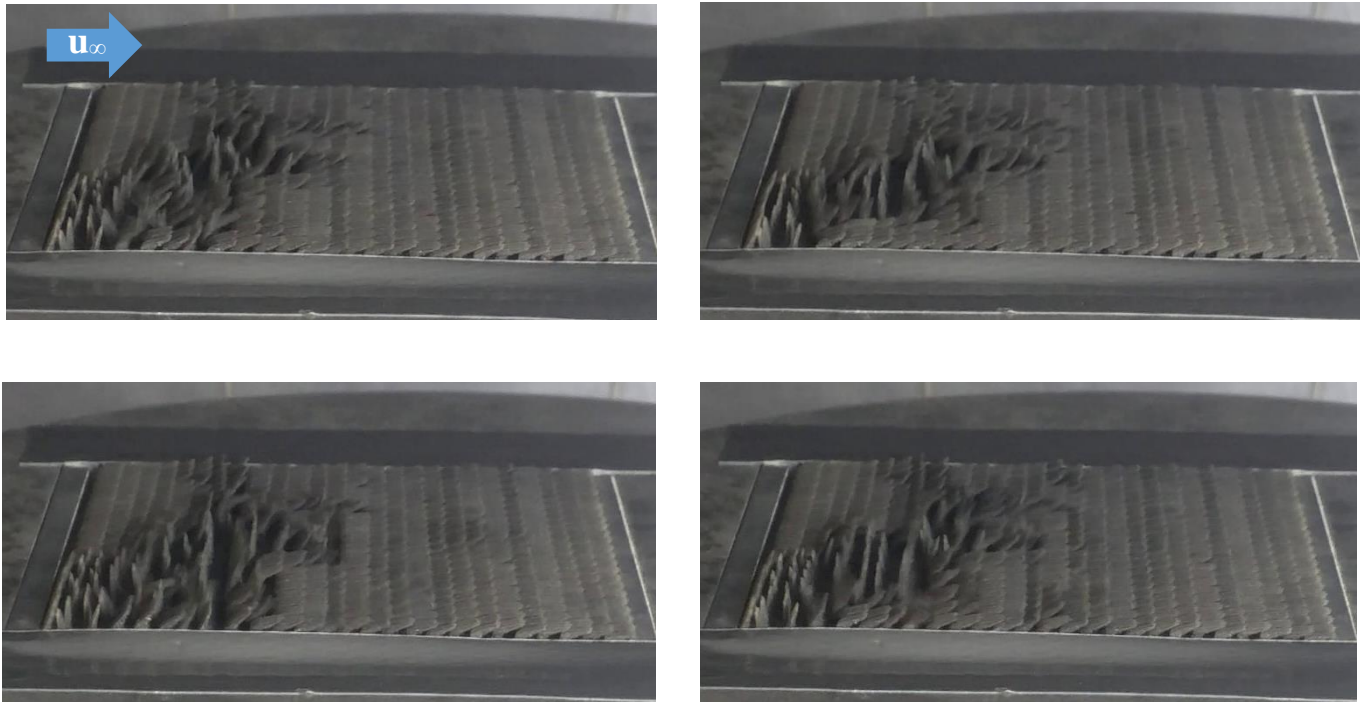


Figure 3.16 Multiple images of fluctuating 3D microflaps 12H downstream of a 1.9 cm fence at 30 m/s

For the 3.8 cm fence, microflaps first began activity at 15 m/s. At this speed, microflaps 12-13H downstream began slight fluctuations from about 0 to 15° at 3 Hz. At 18 m/s, this frequency rose 6 Hz (Fig. 3.17). At 20 m/s, the fluctuations spread to about one-third of the microflaps.

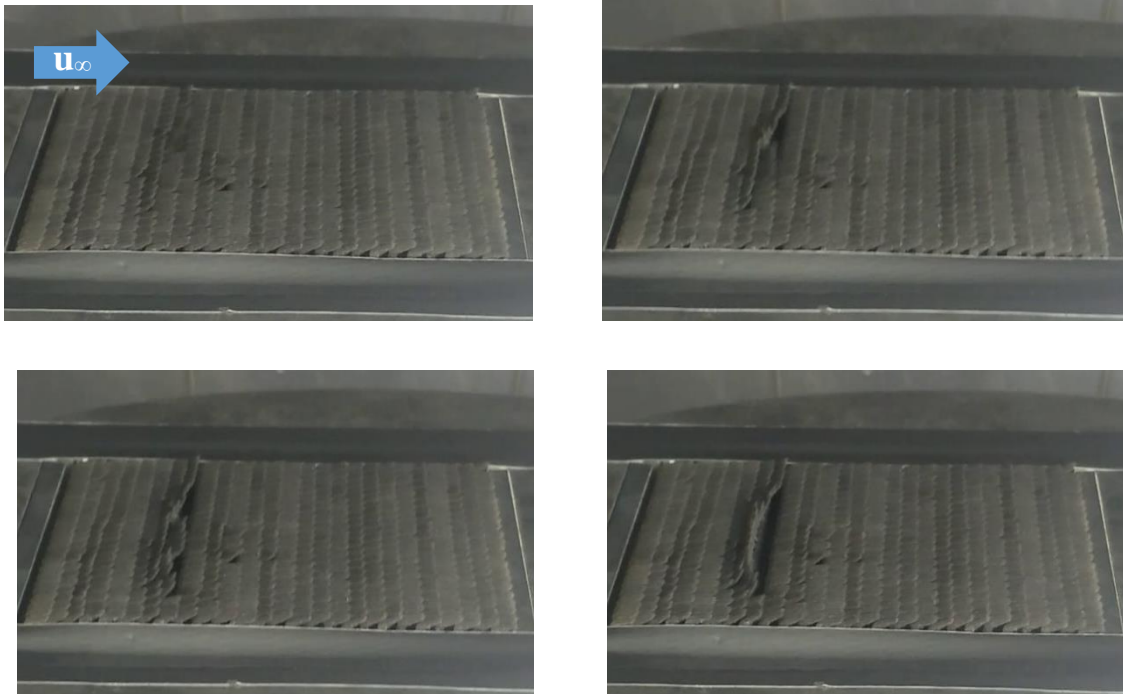


Figure 3.17 Fluctuating 3D microflaps 12H downstream of a 3.8 cm fence at 18 m/s

At 25 m/s, the entire array became very active. Approximately 80% of the microflaps now fluctuated at 9 Hz; microflaps 12-13H downstream fluctuated from 0 to 90° but remained bristled at 40° when not fluctuating, while microflaps 13-14H downstream fluctuated from 0 to 20° but remained flat while not fluctuating (Fig. 3.18). When speed increased to 30 m/s, the microflaps 13-14H downstream fluctuated from 0 to 40°.

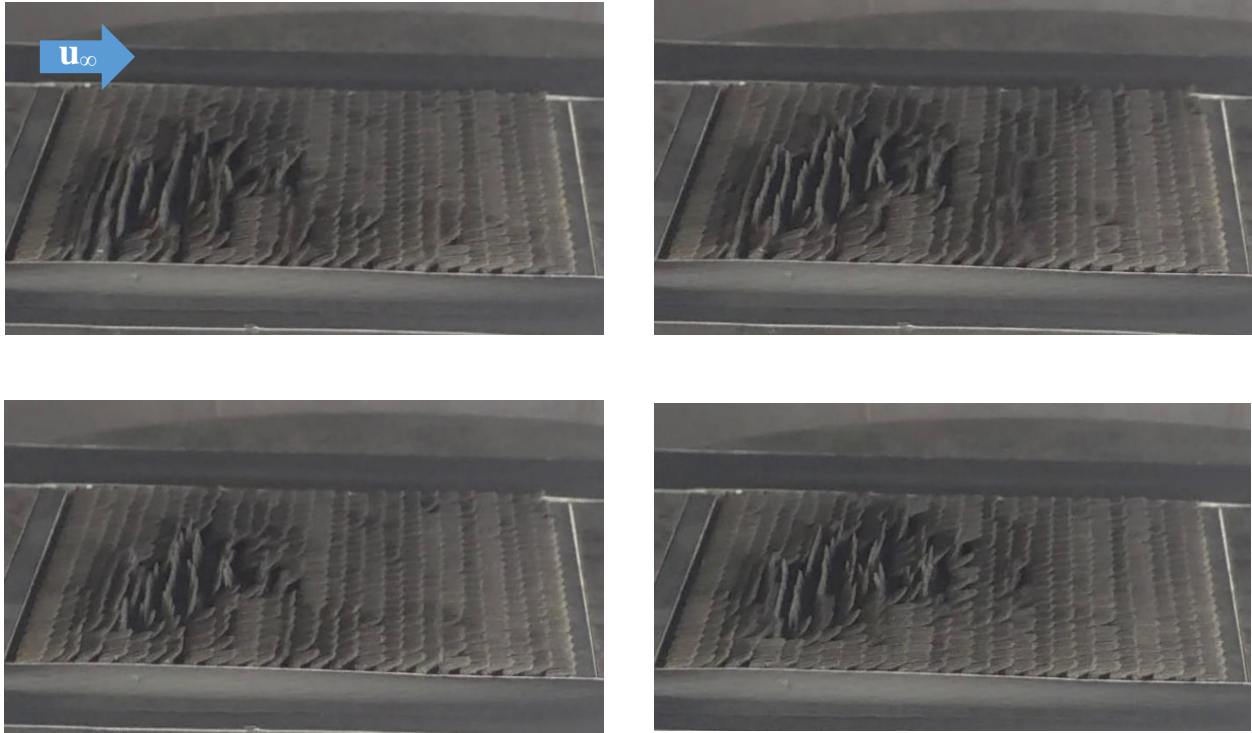


Figure 3.18 Multiple images of fluctuating 3D microflaps 12H downstream of a 3.8 cm fence at 25 m/s

At 12H downstream from the fence, the 3D microflaps were the most active out of all positions. Fluctuation was observed over all microflaps in the array, but was more prevalent in the front half (12-13H downstream) compared to the back half (13-14H downstream). Microflaps located 12-13H downstream stayed bristled when not fluctuating, while microflaps 13-14H downstream stayed flat when not fluctuating. The expected reattachment point of a fence lies in a range from about 10-12H downstream; this region corresponds with the decrease in relative velocity values and larger standard deviation measured downstream of the fence. The reattachment zone of the fence is likely very close to the array position, which would be responsible for the constant changes in flow direction.

3.3.6 Results Upstream of Fence

After testing 3D microflaps downstream of solid fences, the microflaps were placed upstream of the fences. Because the microflap array was a fixed dimension, the front row of the microflaps was $2.66H$ upstream of the 1.9 cm fence and $2H$ upstream of the 3.8 cm fence.

All activity on the microflaps was concentrated in the rows closest to the fence. For the 1.9 cm fence, microflaps first began activity at 15 m/s, where a few microflaps closest to the fence began fluctuating from 0 to 20° at 3 Hz. Additional microflaps bristled as speed increased, and at 30 m/s these microflaps fluctuated at about 5 Hz (Fig. 3.19). No microflap bristling was observed more than $1.06H$ upstream of the fence, and fluctuation was concentrated from 0 - $0.5H$ upstream of the fence.



Figure 3.19 3D microflaps upstream of 1.9 cm fence at 30 m/s

Microflap activity began at similar speeds upstream of the 3.8 cm fence. At 18 m/s, microflaps closest to the fence bristled to approximately 40° and fluctuated at 5 Hz. At 25 m/s the entire row closest to the fence had fully bristled, and by 30 m/s microflaps up to $1H$ upstream bristled (Fig. 3.20). Some bristled microflaps fluctuated from 0 to 40° at this speed.

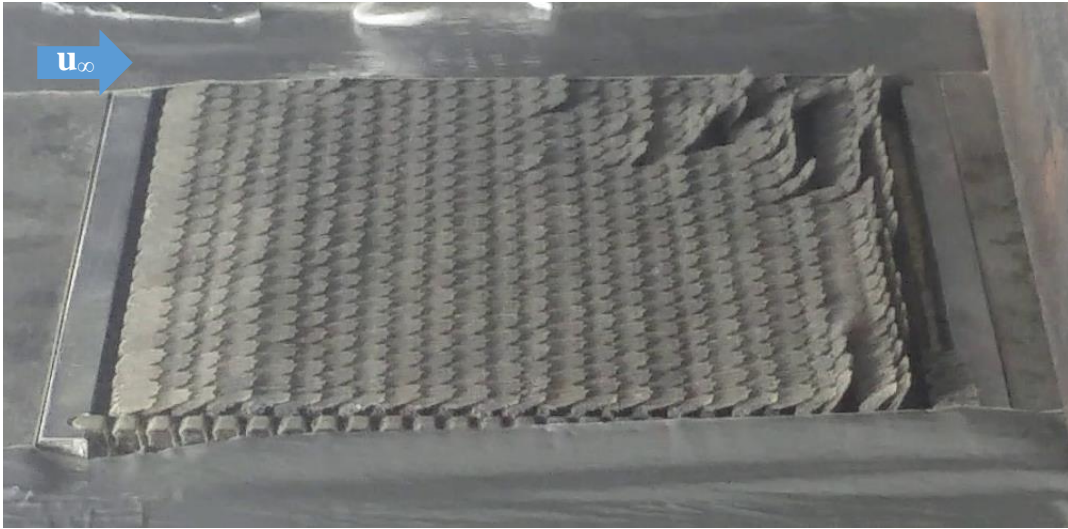


Figure 3.20 3D microflaps upstream of 3.8 cm fence at 30 m/s

The separation bubble upstream of a fence is about $2H$ in length (Orellano and Wengle, 2000). Only microflaps from 0 to $1H$ upstream of the fence were observed to bristle, but bristling was mostly concentrated on rows closest to the fence. Reversed flow velocity more than $1H$ upstream may not have been large enough to cause the microflaps to bristle. Fluctuation of the microflaps was also observed; this is likely due to the close proximity to the upstream reattachment zone of the separated region.

3.4 Suction Plate Results

Tests with the flat plate diffuser with suction consisted of two categories: first, the 3D microflaps were placed underneath the plate and tested at various plate angles, speeds, and suction flow rates; second, the 3D microflaps were placed underneath the flat plate upstream of a 3.8 cm fence. With the 3D microflaps placed at the center of panel 7 and the plate moved as far upstream as possible, the front row of the microflaps was 9.5 cm behind the trailing edge, or

130% of the chord. The plate could be moved up to 26 cm downstream, making the front row of the array at 45% of the chord.

For all tests involving only the plate, the 3D microflaps were not observed to undergo any bristling or fluctuation. Multiple rows of 3 cm tufts were placed underneath and downstream of the plate to gather qualitative information about the flow activity during testing. Tufts showed the most reversal and fluctuation from 10-30% of the chord length downstream from the trailing edge with the plate at 13° and 1300 L/min of suction.

3.4.1 Tuft Results

The first test of the flat plate involved no suction to understand behavior of the tufts at different speeds and angles. Initially, the plate was set to the maximum height from the floor possible, 13.3 cm, with the plate at 0° angle of attack. At a speed of 15 m/s and the plate at 10° , tufts on the plate fluctuated, indicating separation on the plate had occurred. The plate was set to its maximum angle of attack, but no change to the tufts on the floor of the wind tunnel was observed.

The plate was then moved as close to the floor of the wind tunnel as possible, 10 cm. At 10° and 20 m/s with no suction, all tufts underneath the plate began fluctuating from 0 to 20° from the streamwise centerline. Suction was then applied to the plate. At suction flow rates above 1700 L/min, tuft fluctuation was increased to 90° from the centerline.

At 20° angle of attack and 10 m/s, all tufts underneath the plate fluctuated from 0 to 90° at 6 Hz. Suction flow rates above 1300 L/min increased the amplitude of these fluctuations to 180° , indicating brief full reversal of flow over the tufts. This test was repeated with 3D microflaps in place of the tufts, but the microflaps were unable to be bristled at these conditions.

At 20° angle of attack and 15 m/s, the tufts underneath the plate behaved the same as at 10 m/s, however tufts up to 30% of the chord downstream from the trailing edge began exhibiting unsteadiness, fluctuating from 0 to 20°. Suction flow rates greater than 1300 L/min raised this fluctuation amplitude to 180°. 3D microflaps underneath the plate and downstream of it were unable to be bristled. The plate was set to higher angles of attack, up to 45°, and higher speeds, up to 30 m/s, but test results did not differ.

The reasons for the flat plate's inability to create consistent reverse flow are unknown. Dimensionless suction flow rates for the plate were 0.04 at 10 m/s, 0.02 at 20 m/s, and 0.013 at 30 m/s, above the value of 0.01 necessary for full separation control on an airfoil at 18° as found by Huang *et al* (2004). The plenum chamber and hoses attached to the flat plate may have interfered with the ability to control separation or losses through the system may have greater than estimated, thus hindering the plate's ability to induce reverse flow on the floor of the wind tunnel.

3.4.2 Combination Flat Plate and Fence Results

Combining the flat plate with a fence resulted in the 3D microflaps bristling and fluctuating. 3D microflaps were placed directly upstream of a 3.8 cm fence, making the front row 2H upstream of the fence. Microflaps were not placed behind the fence in combination with the plate to preserve interactions between the microflaps and the boundary layer.

As expected, with the plate at 0° angle of attack, increasing plate suction did not affect microflap bristling. At 13° and 10 m/s, microflaps 0-1H upstream of the fence bristled fully. When applying 1300 L/min of suction, bristled microflaps fluctuated from 0 to 30°. Microflaps bristled at about double the upstream distance compared to only the fence at this speed (Fig.

3.21). Increasing suction to 2200 L/min caused additional microflaps to bristle, but did not cause any additional fluctuation.

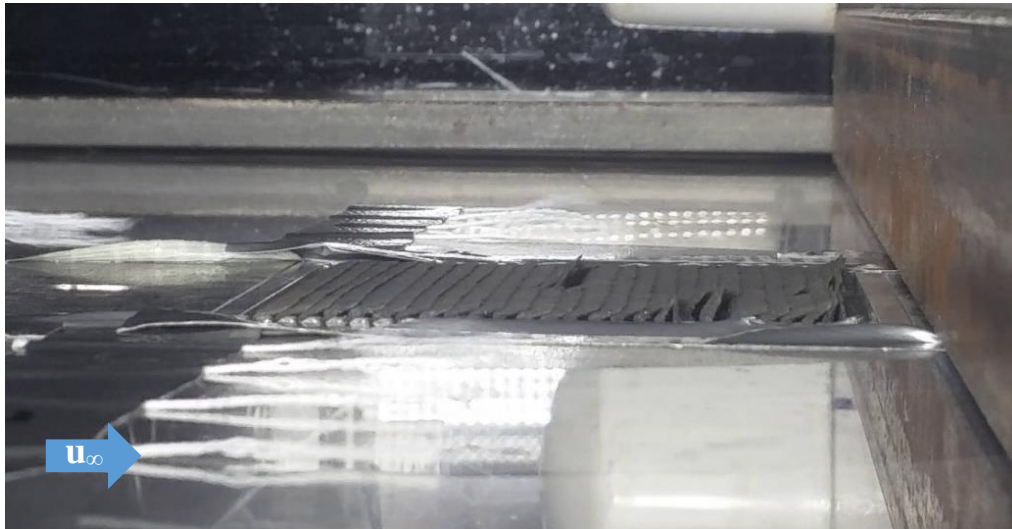


Figure 3.21 3D microflaps upstream of a 3.8 cm fence, at 130% chord length of flat plate set at 13°. 10 m/s and 1300 L/min of suction

At 13° and 15 m/s, microflaps 0-1H upstream of the fence bristled up to 60° (Fig. 3.22 A). Increasing suction to 800 L/min caused fluctuation of these microflaps from 0 to 60° and additional bristling up to 1.45H upstream of the fence (Fig. 3.22 B). At 2000 L/min of suction, approximately one-third of the microflap array had fully bristled, and about half of the bristled microflaps fluctuated from 90 to 30° (Fig. 3.22 C).



Figure 3.22 3D microflaps upstream of a 3.8 cm fence at 130% chord length of flat plate set at 13° . 15 m/s with no suction (A), 800 L/min of suction (B), and 2000 L/min of suction (C)

After removing suction, microflaps did not fall back to the resting position, but fluctuation decreased; only a small number of bristled microflaps continued fluctuating, even after increasing the speed to 20 m/s. At 20 m/s and 1300 L/min of suction, approximately half of the microflaps became fully bristled and fluctuated from 90 to 45° . Increasing suction to 2000 L/min applied this fluctuation to two-thirds of the bristled scales (Fig. 3.23)



Figure 3.23 View of 3D microflaps upstream of a 3.8 cm fence, at 130% of flat plate at 13° . 20 m/s with 2000 L/min of suction.

Combining the 3.8 cm fence with the flat plate diffuser was a successful method of bristling the 3D microflaps. On its own, the plate was unable to actuate any 3D microflaps. Microflaps bristled and fluctuated upstream of the fence alone, but this fluctuation was limited to a few rows just upstream of the fence. Combined, microflaps bristled and fluctuated up to $3.8H$ upstream of the fence, almost double the streamwise distance compared to the fence alone. In the final configuration, about two-thirds of the microflaps could be bristled. The increase in number of microflaps bristled was likely because the plate could increase the size of the separated region upstream of the fence.

3.5 Summary and Microflap Bristling and Fluctuation Analysis

2D microflaps and 3D microflaps bristled in reverse flow velocities between 10-15 m/s. However, only 3D microflaps bristled downstream and upstream of a fence. 3D microflaps bristled up to $1H$ upstream of a fence and from $1-14H$ downstream of a fence. Fluctuation of

microflaps was observed between 1-2H downstream, 8-14H downstream, and 0-0.5H upstream of a fence, as well as from 0-3.8H upstream of a fence combined with suction. Fig. 3.24 shows a schematic of the expected flow behavior in the fence separation bubble compared with the observed microflap behavior.

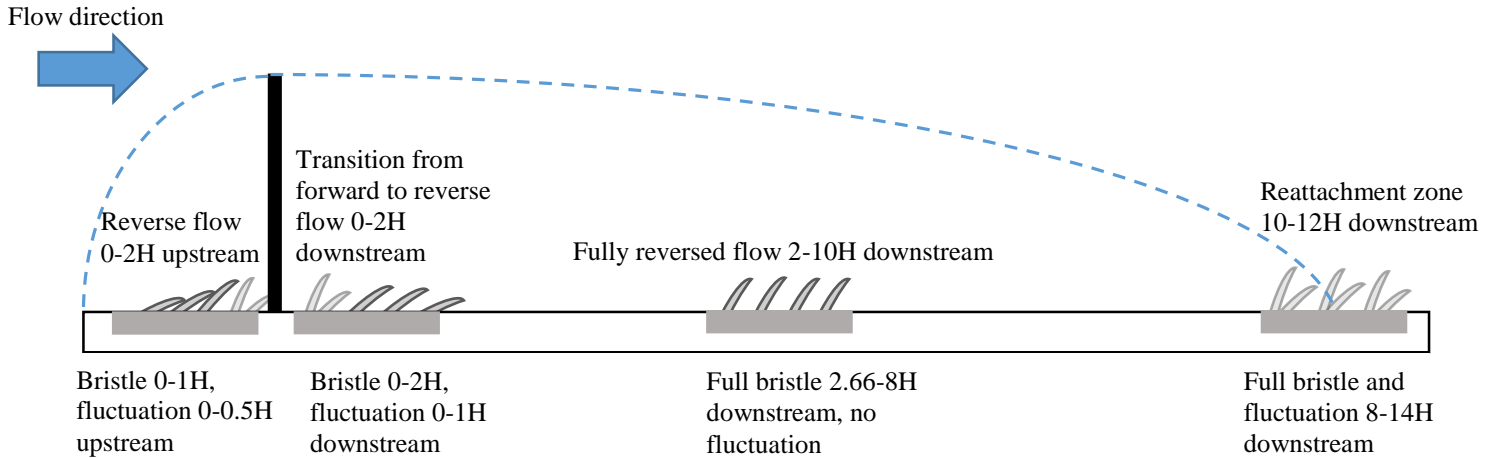


Figure 3.24 Schematic of expected flow behavior and observed microflap behavior upstream and downstream of 2D fence

Using wall velocity values measured downstream of the fence, dynamic pressure of the airflow was calculated (Eq. 17). Dynamic pressure ranged from 10 to 100 Pa at 20 m/s free-stream velocity.

$$q = \frac{1}{2} \rho u^2 \quad (17)$$

When multiplied by the exposed frontal area of the flat microflaps (0.16 cm², approximately 15% of the total microflap area) and distance of this exposed area from the pivot point (2 mm), the estimated moment exerted on microflaps by the airflow was calculated. M_q ranged from 0.25 to 3.31 N-μm at 20 m/s free-stream velocity. This was divided by the expected

moment due to friction between the microflap and the wire to create a nondimensional moment coefficient (Eq. 18). The frictional moment was estimated using the weight of the microflaps (2.7 mN) and the distance of the center of gravity to the pivot point (0.3 mm). However, due to manufacturing differences and additional side friction between microflaps, in reality friction varied across the array. The estimated friction used for moment coefficient calculation was 0.4 N- μ m. When moment coefficient was greater than 1, the microflaps were expected to bristle.

$$M_c = \frac{M_q}{M_{Fr}} \quad (18)$$

Based on these conditions, a moment coefficient of 1 was reached at a dynamic pressure value of 12.28 Pa, corresponding to a velocity of 4.58 m/s, well within the measured relative velocity values downstream of the fence. Using measured velocity values downstream of the fence, at 10 m/s free-stream speed moment coefficient was very close to 1, only slightly exceeding it between 2 and 6H downstream of the fence (Fig. 3.25). No microflaps were observed to bristle at this speed. However, at 20 m/s, the moment coefficient was well above 1 at all streamwise locations; microflaps were observed to bristle at various locations downstream at this free-stream speed. Between 10-12H downstream of the fence, moment coefficient is close to 1 for all three test speeds. Microflaps were observed to constantly fluctuate in this region; flow transitioning between forward and reversed flow may have applied just enough force to bristle the microflaps.

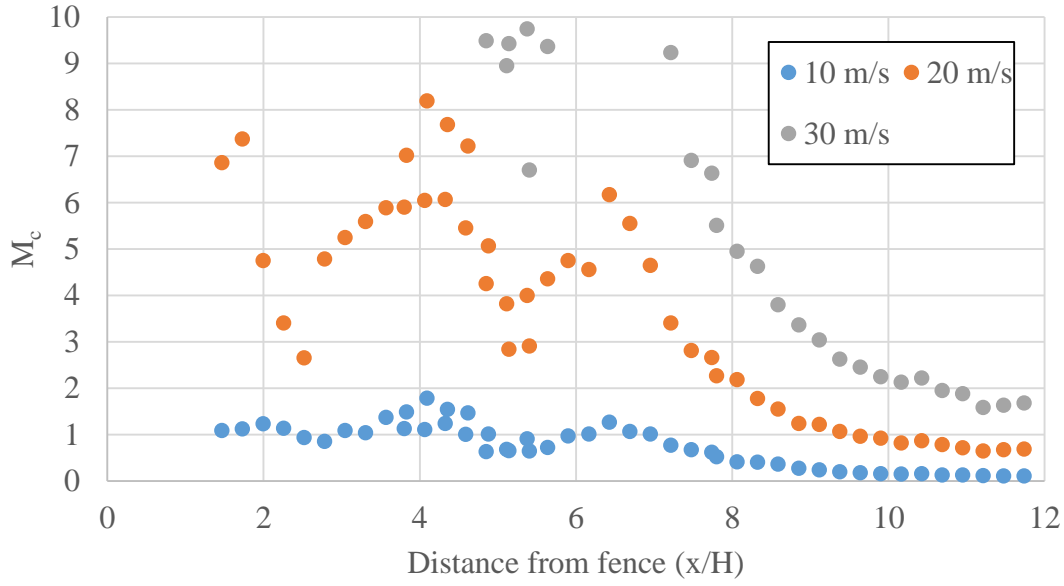


Figure 3.25 Moment coefficient applied to 3D microflaps downstream of 3.8 cm fence

At test speeds where microflap bristling was observed, the minimum dynamic pressure values at bristling locations are between 20 and 50 Pa, or approximately 30 and 80 μN of force applied to the microflap. Free-stream dynamic pressure at 20 m/s is 234 Pa. Mako scales are capable of flow control at dynamic pressure levels as low as 125 Pa (Wheelus, 2015).

3D microflaps were observed to fluctuate upstream and downstream of the 2D fence. However, microflap fluctuation frequency varied across locations and test speeds. To investigate fluctuation further, the Strouhal number of the fluctuating microflaps was calculated using the microflap chord length (0.487 cm), fluctuation frequency, and free-stream velocity (Eq. 19)

$$St = \frac{fc}{u_\infty} \quad (19)$$

Strouhal numbers ranged from 0.001-0.002, indicating some consistency between different test locations and speeds. Generally, as speed increased, microflap fluctuation

frequency increased as well. Mako shark scales may also fluctuate in separated flow conditions; using the calculated Strouhal numbers, mako free-stream swimming speed, and scale chord length of approximately 220 μm (Motta *et al*, 2012), the possible fluctuation frequency of the shark scales could be estimated. For a shark swimming at 10 m/s, scale fluctuation frequency would range from 45-90 Hz. 3D microflap fluctuation frequency ranged from 3 to 12 Hz.

CHAPTER 4: CONCLUSIONS

This thesis consisted of two parts. First, mechanical models of shark scales were designed and manufactured using a 3D printer. A flat plate diffuser with suction was also designed and manufactured for the generation of a separated flow region. Second, these microflaps were tested in a low-speed wind tunnel in both forwards and reverse orientations. Microflaps were placed in separated flow regions generated by the flat plate diffuser and solid fences. A hot film probe was used to gather velocity magnitude measurements downstream of the solid fence. The primary objective of this research was to identify if flow in the lower 5% of the boundary layer could passively actuate microflaps.

Testing confirmed that it is possible for low-momentum flow to actuate both 2D and 3D microflaps. The subsequent tests focused on identifying flow conditions that would cause microflaps to be actuated. 3D microflaps were able to be bristled in separation bubbles generated by a solid fence. After comparing results with previous studies on separation bubbles behind solid fences, 3D microflaps showed the most fluctuation in the reattachment zone. This supports the hypothesis regarding the mechanism of how shark scales could also be passively bristled by reversing flow to control separation as it occurs.

After analyzing velocity profile data, the flow velocity required to bristle the 3D microflaps was identified. The minimum value seen capable of bristling the 3D microflaps was 5.8 m/s, corresponding with a dynamic pressure of 20 Pa. 3D microflaps bristled at backflow

speeds as low as 20% of the free-stream velocity. 3D microflaps required an estimated 30 μN of force to overcome friction and bristle. These relatively low velocity requirements are within expected reverse flow velocities of an object moving at 30 m/s.

The questions posed by this thesis were able to be answered. However, this is only a first step into shark skin-inspired passive separation control in airflow. The microflap designs used in this experiment were the first design iteration, and several issues were identified. These issues included friction between microflaps and hinges preventing some bristling and the tendency of 3D microflaps to over-rotate past their designed bristling angle and become stuck. Future research should focus on improving the microflap design, such as new methods to allow the microflaps to be moved in the boundary layer other than rotating about hinges.

The potential separation control capabilities of microflaps is also an important area of future study. For example, by attaching the current design or an improved version of the 3D microflaps to an airfoil, drag measurements could be made and the performance capabilities of the 3D microflaps could be investigated. These microflaps may have the capability to act as separation control devices. This would be an ideal method of flow control, able to reduce drag without expending energy and engaging only when necessary, as a passive, flow-actuated device.

REFERENCES

- Alrefi, MD, and Acharya, M (1996), "Controlled Leading-Edge Suction for Management of Unsteady Separation over Pitching Airfoils," *AIAA Journal*, Vol 34, No 11, pp 2327-2336.
- Anderson Jr, JD (2010), "Fundamentals of Aerodynamics," *Tata McGraw-Hill Education*.
- Bearman, PW, and Harvey, JK (1976), "Golf Ball Aerodynamics," *The Aeronautical Quarterly*, Vol 27, No 2, pp 112-122.
- Bechert, DW, Hoppe, G, and Reif, W (1985), "On the Drag Reduction of the Shark Skin," *23rd Aerospace Sciences Meeting*.
- Bechert, DW, Bruse, M, Hage, WV, Van der Hoeven, JT, and Hoppe, G (1997), "Experiments on Drag-Reducing Surfaces and their Optimization with an Adjustable Geometry," *Journal of Fluid Mechanics*, Vol 338, pp 59-87.
- Bechert, DW, Bruse, M, and Hage, WV (2000), "Experiments with Three-Dimensional Riblets as an Idealized Model of Shark Skin," *Experiments in Fluids*, Vol 28, No 5, pp 403-412.
- Blackwelder, RF, and Eckelmann, H (1978), "The Spanwise Structure of the Bursting Phenomenon," in "Structure and Mechanisms of Turbulence I", *Springer, Berlin, Heidelberg*, pp 190-204.
- Choi, J, Woo-Pyung, J, and Choi, H (2006), "Mechanisms of Drag Reduction by Dimples on a Sphere," *Physics of Fluids*, Vol 18, No 4, 041702
- Dennel, R (1997), "The World's Oldest Spears," *Nature*, Vol 385, No 6619, pp 767-768.
- Devey, SP, and Hancock, RL (2016), "Aerodynamic Force Study on an Airfoil Covered with Shark Skin," AIAA Region II student conference paper, presented April 2016 in Huntsville, AL.
- Fischer, MC, Wright Jr, AS, and Wagner, RD (1983), "A Flight Test of Laminar Flow Control Leading-Edge Systems."
- Gad-el-Hak, M (2000), "Flow Control: Passive, Active, and Reactive Flow Management," *Cambridge University Press, Cambridge*.

- Hammerton, J and Lang, AW (2015), "First Signs of Flow Reversal Within a Separated Turbulent Boundary Layer," *APS Meeting Abstracts*, Vol 60.
- Huang, L, Huang, PG, LeBeau, RP, and Hauser, T (2004), "Numerical Study of Blowing and Suction Control Mechanism on NACA 0012 Airfoil," *Journal of Aircraft*, Vol 41, No 5, pp 1005-1013.
- Kim, HT, Kline, SJ, and Reynolds, WC (1971), "The Production of Turbulence Near a Smooth Wall in a Turbulent Boundary Layer," *Journal of Fluid Mechanics*, Vol 50, No 1, pp 133-160.
- Klebanoff, PS (1954), "Characteristics of Turbulence in a Boundary Layer with Zero Pressure Gradient," NACA Report No R-1247, Washington, D.C.
- Kline, SJ, Reynolds, WC, Schraub, FA, and Runstadler, PW (1967), "The Structure of Turbulent Boundary Layers," *Journal of Fluid Mechanics*, Vol 30, No 4, pp 741-773.
- Koga, DJ (1983), "Control of Separated Flowfields Using Unsteadiness," Ph.D. Dissertation, *Illinois Institute of Technology, Chicago*.
- Lang, AW, Motta, P, Hidalgo, P, and Westcott, M (2008), "Bristled Shark Skin: a Microgeometry for Boundary Layer Control?," *Bioinspiration & Biomechanics*, Vol 3, No 4, 046005.
- Lang, AW, Habegger, P, Hueter, ML, and Afroz, F (2011), "Shark Skin Separation Control Mechanisms," *Marine Technology Science Journal*, Vol 45, No 4, pp 208-215.
- Lang, AW, Bradshaw, MT, Smith, JA, Wheelus, JN, Motta, PJ, Habegger, ML, and Hueter, RE (2014), "Movable Shark Scales Act as a Passive Dynamic Micro-Roughness to Control Flow Separation," *Bioinspiration & Biomimetics*, Vol 9, No 3, 036017.
- Martin, A (2001), "The Origins of Modern Sharks," accessed Sep. 22, 2017, retrieved from http://www.elasmo-research.org/education/evolution/origin_modern.htm.
- Miau, J Chou, JH, Lee, KC, and Chen, MH (1991), "Control of Separated Flow by a Two-Dimensional Oscillating Fence," *AIAA Journal*, Vol 29, No 7, pp 1140-1148.
- Mohammed-Taifour, A, Schwaab, Q, Pionon, J, and Weiss, J (2015), "A New Wind Tunnel for the Study of Pressure-Induced Separation and Reattaching Flows," *The Aeronautical Journal*, Vol 119, No 1211, pp 91-108.
- Motta, P, Habegger, ML, Lang, A, Hueter, R, and Davis, J (2012), "Scale Morphology and Flexibility in the Shortfin Mako *Isurus Oxyrinchus* and the Blacktip Shark *Carcharhinus Limbatus*," *Journal of Morphology*, Vol 273, No 10, pp 1096-1110.

- National Instruments Corporation (2007), "User Guide and Specifications, NI USB-9211/9211A".
- Orellano, A, and Wengle, H (2000), "Numerical Simulation (DNS and LES) of Manipulated Turbulent Boundary Layer Flow Over a Surface-Mounted Fence," *European Journal of Mechanics-B/Fluids*, Vol 19, No 5, pp 765-788.
- Patrick, W (1987), "Mean Flowfield Measurements in a Separated and Reattached Flat-Plate Turbulent Boundary Layer," NACA Contractor Report No 4052.
- Prandtl, L, "On Fluid Motions with Very Small Friction" (1904), *Verhldg*, 3, pp 484-91.
- van Rantingen, SW, de Jong, AT, and Gousseau, P (2013), "PIV Measurements of the Flow Behind a 2D Fence in an Atmospheric Boundary Layer Wind Tunnel," *Proceedings of the 6th European and African Conference on Wind Engineering*, July 2013, pp 1-4.
- Reif, WE (1985), Squamation and Ecology of Sharks," *Courier Forschungsinstitut Senckenberg*, Vol 78, pp 1-255.
- Siefert, A, Bachar, T, Koss, D, Shepshelovich, M, and Wygnanski, I (1993), "Oscillatory Blowing: a Tool to Delay Boundary-Layer Separation," *AIAA Journal*, Vol 31, No 11, pp 2052-2060.
- Smith, CR, Sabatino, DR, Praisner, TJ, Seal, CV (2012), "Hydrogen Bubble Flow Visualization," in "Flow Visualization: Techniques and Examples," pp 27-42.
- Sreenivasan, KR (1987), "Turbulence, Turbulence Control, and Drag Reduction," YALE UNIV NEW HAVEN CT MASON LAB.
- Wheelus, JN (2015), "An Investigation of the Flow Control Mechanisms of Shortfin Mako Shark Skin," Ph.D. Dissertation, *The University of Alabama, Tuscaloosa*.
- White, FM (2008), "Fluid Mechanics, Seventh Edition," *McGraw-Hill, Boston*.